Modeling and Inversion of Cross-Well Electrical Resistivity Tomography Data

Submitted in partial fulfilment of the requirements for the degree of

Master of Science

By

Nimatullah

Roll No. – 22N0005

M.Sc. Applied Geophysics

Under the supervision of

Prof. Anand Singh

Department of Earth Sciences

Indian Institute of Technology Bombay

2024

Approval Sheet

The M.Sc. dissertation report entitled **"Modeling and Inversion of Cross Well Electrical Resistivity Tomography data"** prepared by Nimatullah (Roll No. – 22N0005) is hereby approved for submission.

Prof. Anand Singh
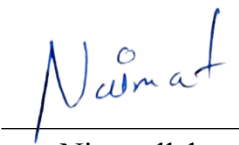
(Supervisor)

Prof. Mohan Gollapally

(Examiner)

Prof. Anand Singh

(Examiner)

Declaration

I hereby affirm that this written submission is a true representation of my own thoughts and ideas, expressed in my own words. In instances where I have incorporated the ideas or words of others, I have diligently cited and referenced the original sources. Furthermore, I attest that I have upheld all principles of academic honesty and integrity throughout the creation of this submission. I have not engaged in any misrepresentation, fabrication, or falsification of ideas, data, facts, or sources. I acknowledge that any breach of these principles may result in disciplinary measures from the Institute and potential legal consequences from sources that have not been appropriately cited or from which proper permissions have not been obtained as required.

Nimatullah

Acknowledgments

I want to express my gratitude for the chance to work on this project and give a big thanks to Professor Anand Singh for believing in me and guiding me every step of the way. His advice has been invaluable, and I couldn't have done it without him.

I also want to thank the lab and support staff for providing us with everything we needed to get the job done. Their help made a huge difference.

And of course, a big shoutout to my friends and family for always being there for me, cheering me on, and helping me through any challenges that came up. I couldn't have finished this project without their support.

Table of Contents

List of Figures

Figure 1. 1 Current is injected via current electrodes 1 and 2, while voltage readings are taken at potential electrodes 1 and 2. This visualization encapsulates the fundamental process of DC resistivity measurement, elucidating the connection between injected current and recorded voltage. Such an approach provides insights into the electrical properties of the system under study _____ 1

Figure 1. 2 We present the graphical representations of Vertical Electrical Sounding (VES), displaying distinct curves for both the A-type and H-type configurations. Panel (a) depicts the characteristic curve for the A-type VES, while Panel (b) illustrates the curve for the H-type VES. These curves serve as graphical interpretations of the electrical resistivity measurements obtained through the VES method, offering insights into subsurface geological features and stratifications. The distinct shapes and trends of these curves provide valuable information about the electrical properties of the Earth's subsurface, aiding in geological and geophysical investigations _____ 3

Figure 1. 3 plunges into the depths of the Wenner array setup, where 'a' signifies the electrode spacing, offering a glimpse into the arrangement's intricacies. This is further complemented by an exploration of the electric field distribution beneath, meticulously captured and analyzed by N. Wiwattanachang in 2011, revealing the nuanced dynamics of subsurface electrical properties (Wiwattanachang and Giao, 2011) _____ 4

Figure 1. 4 Electrode locations and their corresponding collected data using the Wenner configuration (Wilson, et al, 2022)_____ 5

Figure 1. 5 . Contour plot of the collected apparent resistivity data (Wilson, et al, 2022) ____ 5

Figure 1. 6 Schematic diagram of the deep-towed marine electrical resistivity tomography system. Two current electrodes C1 and C2 and eight potential electrodes P1–P8 are attached to the cable together with two reference electrodes COM1 and COM2 (Ishizu, et al, 2019) _ 6

Abstract

This thesis delves into the advancements and applications of electrical resistivity methods, particularly focusing on cross-well Electrical Resistivity Tomography (ERT) for subsurface imaging. Traditional direct current (DC) resistivity methods provide valuable insights into subsurface resistivity distributions, but with limitations in depth penetration and resolution. To overcome these limitations, the study presents a novel approach utilizing cross-well ERT, which involves strategically placed electrodes within boreholes for enhanced depth penetration and resolution.outlines the methodology and data acquisition techniques, including vertical electrical sounding, imaging, continuous profiling, and cross-well ERT, along with their respective applications. Noise analysis and removal techniques are discussed, followed by forward modeling methodologies using finite element methods and mesh generation strategies. Two synthetic models are presented to simulate CO_2 injection and spread within homogeneous and heterogeneous subsurface mediums, demonstrating the dynamic behavior and impact of CO_2 within controlled environments. The inversion process for cross-well ERT data is detailed, including the choice of norm, minimization of inverse problems, and inversion results for the presented models. In summary, this study contributes to the advancement of subsurface imaging techniques, particularly in the context of CO_2 monitoring and geological investigations. The utilization of cross-well ERT offers promising avenues for detailed subsurface imaging, with implications for various fields such as environmental monitoring, geological exploration, and hazard assessment.

Chapter-1

Introduction

1.1 DC Resistivity Methods

The direct current (DC) resistivity method measures subsurface resistivity. In this method, we inject electric currents into the ground and measure electric voltages at different locations; the method gives information about the distribution of electrical resistivity in the subsurface. The apparent resistivity (ρ_a) is calculated by measuring the potential difference (ΔV) between different pairs of electrodes, considering the current (I) and a geometric factor (G) specific to the electrode array used.

$$\rho_a = \frac{G\Delta V}{I} \qquad (1.1)$$
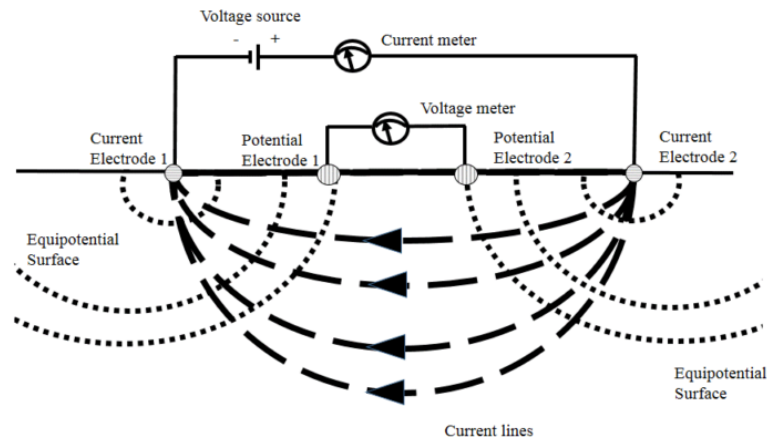
Figure 1. 1 Current is injected via current electrodes 1 and 2, while voltage readings are taken at potential electrodes 1 and 2. This visualization encapsulates the fundamental process of DC resistivity measurement, elucidating the connection between injected current and recorded voltage. Such an approach provides insights into the electrical properties of the system under study

However, the measured data alone do not directly offer the desired information. To extract meaningful insights, inversion techniques are essential. The inverse DC resistivity problem is inherently challenging due to the problem is ill-posed concerning data errors and incomplete data sets. Initially, resistivity soundings were employed to assess horizontal layers of varying conductivity. Modern advancements involve profile measurements using pre-installed multielectrode lines, offering good observation for investigating 2-D structures. For

3-D exploration, large electrode arrays or numerous parallel profile lines are employed to facilitate comprehensive investigations.

Despite these advancements, the depth of penetration and resolution of DC 3D resistivity methods have limitations. In this study, we present a novel approach focusing on Modelling and Inversion of Cross-Well Electrical Resistivity Tomography (ERT) data. This method involves drilling boreholes and placing electrodes within them, following the same principles as the DC resistivity method.

By adopting a cross-well ERT approach, we aim to overcome the limitations of traditional DC 3D resistivity methods. The utilization of boreholes and strategically placed electrodes enhances depth penetration and resolution, making it a promising avenue for detailed subsurface imaging. Our study contributes to advancing the understanding of subsurface structures through innovative modeling and inversion techniques, paving the way for improved accuracy and reliability in geological investigations.

1.2 Data Acquisition

1.2.1 Vertical electrical sounding

A vertical electrical sounding array is technique for data acquisition, involving the placement of two current electrodes (AB) and two potential electrodes (MN). These electrodes are initially positioned at the midpoint and varied distances. The survey progresses by moving the current electrodes outward, while the potential electrodes are kept stationary until the measured voltage reaches a threshold too small to be accurately recorded. This systematic approach allows for the collection of meaningful data across different depths, contributing to a comprehensive vertical profile of subsurface electrical resistivity.
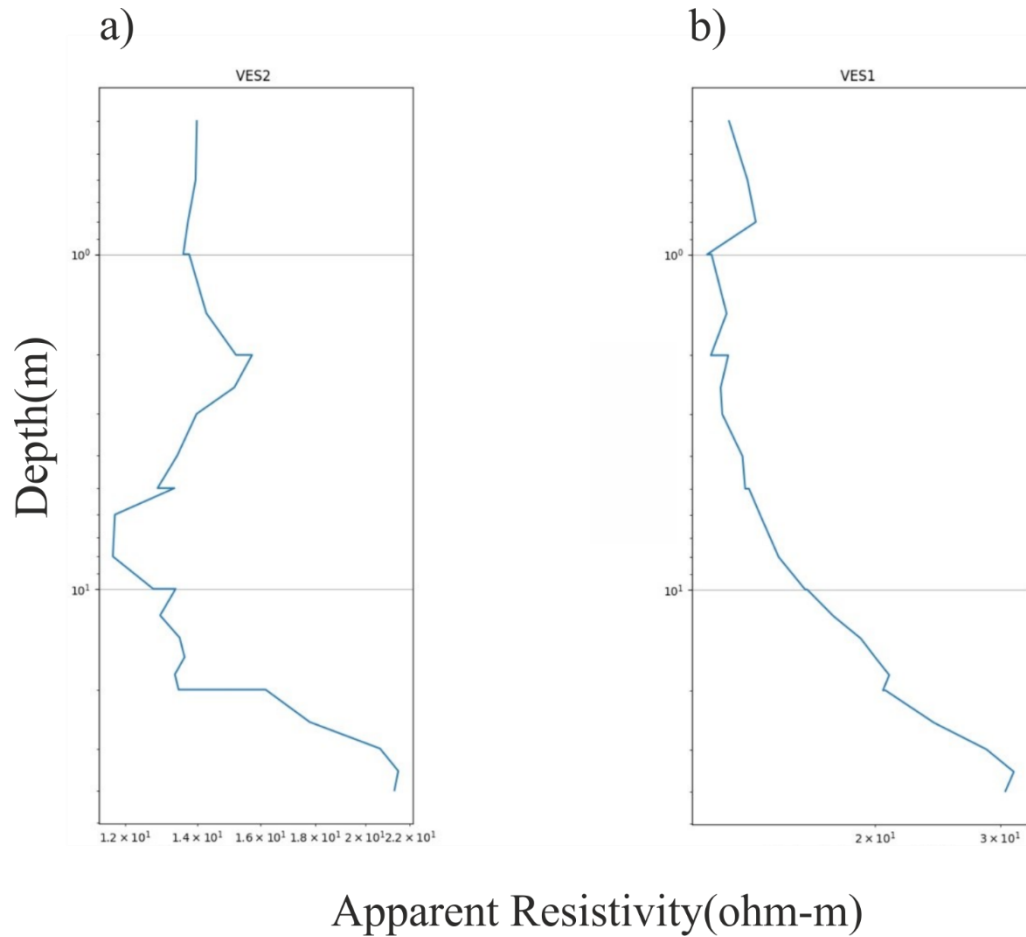
Figure 1. 2 We present the graphical representations of Vertical Electrical Sounding (VES), displaying distinct curves for both the A-type and H-type configurations. Panel (a) depicts the characteristic curve for the A-type VES, while Panel (b) illustrates the curve for the H-type VES. These curves serve as graphical interpretations of the electrical resistivity measurements obtained through the VES method, offering insights into subsurface geological features and stratifications. The distinct shapes and trends of these curves provide valuable information about the electrical properties of the Earth's subsurface, aiding in geological and geophysical investigations

1.2.1.1 Application of VES

- Identifying unsaturated and saturated layers: VES can identify unsaturated and saturated layers below the surface and aquifer potential. (Sikandar, et al, 2010)
- Mapping pipeline routes: VES can be used to map pipeline routes. (Okiongbo, et al, 2013)

1.2.2 Imaging

The Wenner electrode array is a soil resistivity measurement technique, having four electrodes A, M, N, and B. These electrodes are arranged in a straight line at equal intervals. The outer electrodes, A and B, work as current electrodes, while the inner electrodes, M and N, function as potential electrodes. This method gives lateral variations in subsurface resistivity. Widely applied in mineral prospecting, it proves particularly valuable for identifying shear zones, faults, and localized areas exhibiting anomalous conductivity. The simplicity and effectiveness of the Wenner electrode array make it a preferred choice for investigations into the electrical properties of the subsurface.
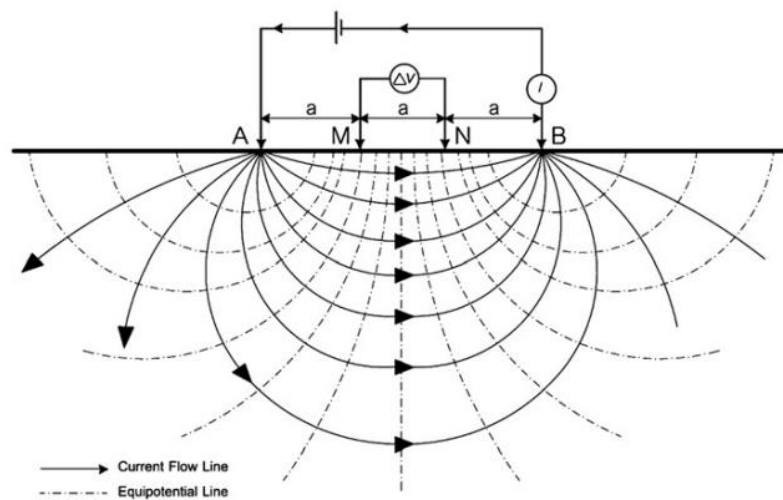
Figure 1. 3 plunges into the depths of the Wenner array setup, where 'a' signifies the electrode spacing, offering a glimpse into the arrangement's intricacies. This is further complemented by an exploration of the electric field distribution beneath, meticulously captured and analyzed by N. Wiwattanachang in 2011, revealing the nuanced dynamics of subsurface electrical properties (Wiwattanachang and Giao, 2011)

Figure 1. 4 Electrode locations and their corresponding collected data using the Wenner configuration (Wilson, et al, 2022)
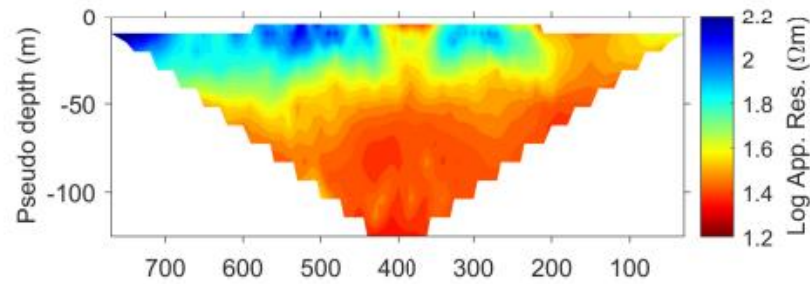
Figure 1. 5 . Contour plot of the collected apparent resistivity data (Wilson, et al, 2022)

1.2.2.1 Application of Imaging
- Imaging is often applied for mapping the resistivity of subsurface materials, helping to distinguish between different soil types and identify bedrock layers. (Adeeko and Samson, 2018)
- In environmental investigations, Imaging can be used to assess the subsurface structure for contamination and monitor groundwater movement. (Masood, et al, 2022)

1.2.3 Continuous profiling

Electrical Resistivity Tomography (ERT) has found applications in terrestrial environments, shallow water regions, and even deep-sea areas. In conducting an ERT survey, an electrical current is introduced between two electrodes, and the resulting voltages are measured across other paired electrodes. The trailing section in this system, known as the long tail, comprises cables with lengths
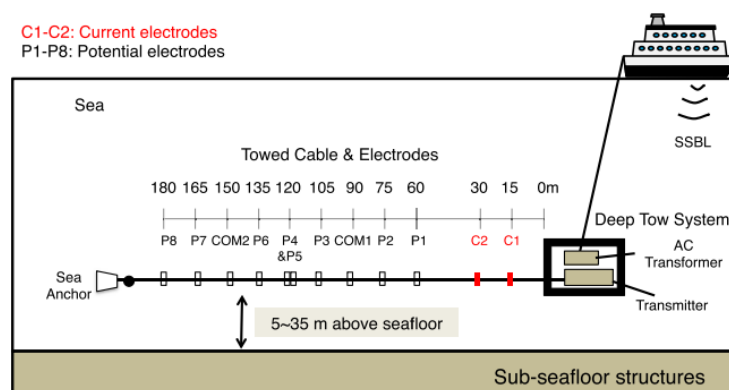
Figure 1. 6 Schematic diagram of the deep-towed marine electrical resistivity tomography system. Two current electrodes C1 and C2 and eight potential electrodes P1–P8 are attached to the cable together with two reference electrodes COM1 and COM2 (Ishizu, et al, 2019)COM2 (Ishizu, et al, 2019)
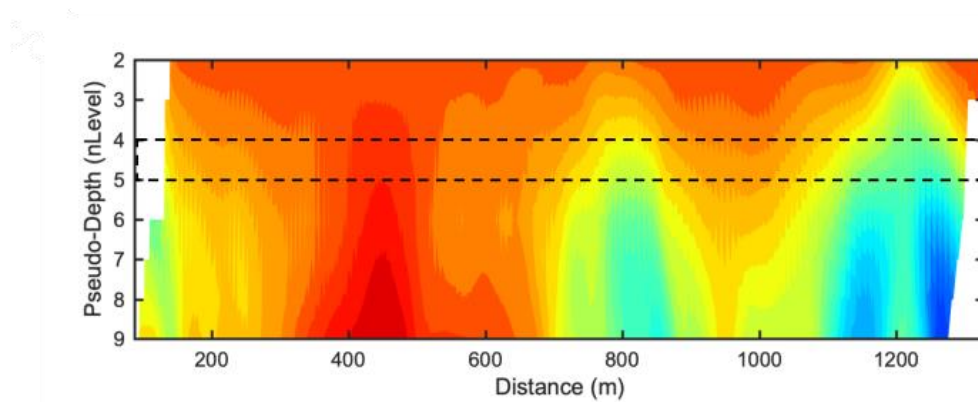
Figure 1. 8 Pseudo-section of the response from the inverted model (Ishizu, et al, 2019)

1.2.3.1 Application of Continuous profiling

- Identification of submarine groundwater discharge (SGD) (Krishan, et al, 2015)
- Mapping of fresh/saline-water intrusion (Nassir, et al, 2015)

1.2.4 Cross-well ERT

Several electrodes are placed in each hole in electrical contact with the formation (see Figure). Two adjacent electrodes are driven by a known current, and the resulting voltage difference is measured between all other adjacent pairs of electrodes (in both boreholes). Then, the known current is applied to two other adjacent electrodes and the voltage is again measured between all other adjacent pairs. This process is repeated until current has been applied to all pairs of adjacent electrodes (in both boreholes).
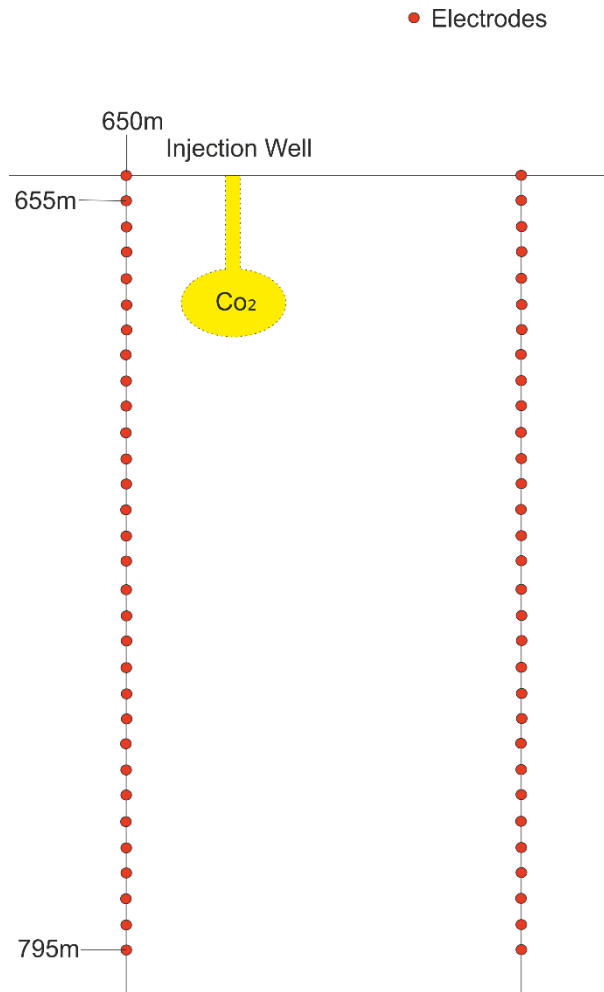
Figure 1. 9 the red circles denote the exact positions of electrodes, strategically situated to fulfill specific roles. Within two boreholes, these electrodes facilitate both current injection and potential measurement. Spanning depths from 650m to 795m, a total of 30 electrodes are meticulously arranged, enhancing the precision of data collection. Furthermore, a dedicated borehole is reserved exclusively for CO2 injection. This comprehensive electrode setup enables meticulous monitoring and analysis of subsurface dynamics, providing invaluable insights into geological phenomena and environmental impacts.

1.2.4.1 Application of cross well ERT

- Monitoring Carbon Dioxide Sequestration using Electrical Resistance Tomography (Newmark, et al, 2003)
- Cross Well Electrical Resistivity Tomography (ERT) Monitoring for Landslides (Tsai, et al, 2021)

1.2.4 Cross-well ERT

Several electrodes are placed in each hole in electrical contact with the formation (see Figure). Two adjacent electrodes are driven by a known current, and the resulting voltage difference is measured between all other adjacent pairs of electrodes (in both boreholes). Then, the known current is applied to two other adjacent electrodes and the voltage is again measured between all other adjacent pairs. This process is repeated until current has been applied to all pairs of adjacent electrodes (in both boreholes).

Carbon capture and storage (CCS) has gained widespread recognition as an effective means of mitigating carbon dioxide (CO_2) emissions amid the escalating global climate crisis. During the process of storing CO_2 in underground reservoirs, the implementation of robust monitoring measures to track changes in the distribution of underground CO_2 can facilitate the evaluation of the effectiveness and safety of carbon sequestration. Cross-borehole electrical resistivity tomography (ERT), as a form of electromagnetic method, exhibits high sensitivity to deeper pore fluids and rock structures (Daily and Owen, 1991), which offers advantages such as ease of implementation, nondestructiveness, cost-effectiveness, and high resolution (Binley, 2005); moreover, ERT provides valuable spatiotemporal information on changes within the underground storage area (Falcon-Suarez, et al, 2017). Consequently, it has found extensive applications in diverse domains, including groundwater resource investigation (Chen, 2022), mineral resources exploration (Prakash and Bharati, 2022), and geological disaster prediction (Adhikari, et al, 2016).

Currently, significant progress in ERT has been achieved in CO_2 storage projects (Carrigan, et al, 2013).For instance, the Ketzin pilot CO_2 project in Germany demonstrated that CO_2 injection generated a substantial electrical signal in the downhole electrode, which facilitated the real-time monitoring of the downhole potential electrode (Schmidt-Hattenberger, et al, 2013); moreover, the joint inversion of seismic and resistivity tomography reveals an approximately twofold increase in resistivity resulting from CO_2 injection (Wagner, et al, 2018). The permanently installed monitoring electrodes in wells demonstrate the effective detection of minute amounts of injected CO_2 in the CaMI project in Canada (Li, et al, 2022). Likewise, during the Svelvik CO_2 Field Lab experiment, four electrodes were placed at a depth of 100 m, facilitating the successful monitoring of the impacts of CO_2 injection on formation saturation and pore pressure (Raab, et al, 2020)

Future Objective:

The future objective of this research is to advance the utilization of cross-well Electrical Resistivity Tomography (ERT) as a robust and versatile technique for detailed subsurface imaging, with a specific emphasis on its application in monitoring and mitigating CO_2

emissions. This objective will be pursued through a multifaceted approach aimed at refining and validating the methodology, data acquisition techniques, and inversion methodologies outlined in the initial study.

- **Methodology Refinement**: Building upon the existing framework, the objective is to refine the methodology for cross-well ERT data acquisition and analysis. This will involve optimizing electrode configurations, refining measurement protocols, and exploring innovative approaches for enhancing depth penetration and resolution. Special attention will be given to addressing practical challenges encountered during field deployments, such as borehole logistics and environmental factors.

- **Advanced Noise Analysis and Removal Techniques**: To improve the signal-to-noise ratio of cross-well ERT data, advanced noise analysis and removal techniques will be developed and implemented. This will involve investigating the sources of noise in different subsurface environments and developing tailored strategies to mitigate their effects. The objective is to enhance the reliability and accuracy of subsurface imaging results, particularly in complex geological settings.

- **Validation through Real-World Experiments**: The future objective includes conducting extensive real-world experiments and field studies to validate the efficacy of cross-well ERT in diverse subsurface environments. These experiments will involve monitoring CO_2 injection and migration processes in both controlled laboratory settings and natural field sites. The objective is to demonstrate the capability of cross-well ERT to accurately image the dynamic behavior of CO_2 within heterogeneous subsurface mediums.

- **Inversion Methodology Enhancement**: Further development and enhancement of inversion methodologies will be pursued to improve the accuracy and efficiency of subsurface imaging. This will involve exploring alternative regularization techniques, investigating the sensitivity of inversion results to parameter selection, and refining algorithms for model parameterization. The objective is to streamline the inversion process and enhance the interpretability of cross-well ERT results.

- **Validation in Diverse Applications**: The objective is to validate the practical utility of cross-well ERT in diverse applications beyond CO_2 monitoring, including environmental monitoring, geological exploration, and hazard assessment. This will involve collaborating with stakeholders from various industries to address specific challenges and demonstrate the versatility of cross-well ERT as a subsurface imaging tool.

Chapter-2

Processing and Forward Modelling

2.1 Processing of Cross-Well Electrical Resistivity Tomography Data

After acquiring field data, the next step involves converting resistance measurements into their respective apparent resistivities. To ensure the accuracy of the resulting model, the data must be of high quality, and devoid of any noise interference. Processing entails the meticulous removal of such noise and refining the data to extract the desired, usable information.

2.2 Noise in Cross-Well Electrical Data

Electrical resistivity tomography (ERT) surveys are relatively insensitive to urban noise. However, background electrical noise can affect the imaging resolution of ERT surveys.

1. **Wellbore Effects:** The condition of the boreholes and the materials used in the wells can influence the measurements. Irregularities in the wellbore, changes in casing material, or the presence of conductive fluids can affect the resistivity measurements. (Bing and Greenhalgh, 2000)

2. **Temperature and Pressure Changes:** Variations in temperature and pressure within the subsurface can impact the resistivity measurements. These changes may be related to seasonal variations, pumping activities, or other environmental factors. (Hayley, et al, 2007)

3. **Instrumentation Noise:** Noise originating from the measurement equipment itself, including the electrodes and cables used, can introduce errors. Regular calibration and maintenance of the instruments are essential to minimize this type of noise. (La Brecque, et al, 2007)

2.3 Noise Removal

Before proceeding with data inversion for cross-well applications, it's essential to conduct a thorough noise analysis.

Outlined below are several recommended processing steps tailored for cross-well scenarios:

- Establish a suitable range of apparent resistivities pertinent to the specific geological setting and operational conditions, and retain data falling within this range.

- Exclude data points exhibiting excessively large standard deviations, as these may indicate potential noise contamination.

- Discard data associated with very low current values, as such readings can be indicative of noise or poor signal quality.

- Eliminate data points linked to negative or extremely small voltage readings, which could skew the accuracy of the subsequent inversion.

- Implement manual inspection and removal of any evidently erroneous or unreliable data points identified through rigorous scrutiny.

2.3 Forward modelling

2.3.1 Finite element methods (FEM)

The Finite Element Method (FEM) is well-suited for simulating resistivity distribution in the subsurface, as it can handle complex geometries and heterogeneous media effectively (Bing and Greenhalgh, 2001). FEM are commonly used to model electrical resistance measurements in 2D cross-well configurations. Generating a finite element mesh (FEM) is a crucial step in this process. In 2D ERT modeling, rectangular or triangular elements are typically employed. However, for cross-well applications, triangular elements are often preferred due to their ability to better capture the geometry of the subsurface between the boreholes.

This study utilizes triangular mesh elements to provide flexibility in mesh refinement, particularly around small-scale features such as fractures, boreholes, and electrodes. Additionally, triangular elements facilitate the incorporation of topography into the model. This approach enhances the accuracy of the electrical resistance measurements in the cross-well setup.

Importance of Unstructured Triangle Meshes:

We found a better way to organize our data called unstructured triangle meshes. They help us describe complex shapes more easily and refine our calculations where needed.
By using these meshes, we can make our calculations much more accurate while using fewer resources.

2.3.2 Calculation of the total potential

Control Equation: The fundamental equation governing the resistivity model involves the relationship between current density (J), electric field strength (E), electrical conductivity (σ), and electric potential (u). This relationship is expressed as:

$$J = \sigma E \tag{2.1}$$

$$E = -\nabla U \tag{2.2}$$

$$\nabla \cdot J = \partial e / \partial t \tag{2.3}$$

$$\nabla \cdot (\sigma \nabla u) = -2I \cdot \delta(A) \tag{2.4}$$

Here, J represents the current density (A/m²), E denotes the electric field strength (V/m), σ is the electrical conductivity (S/m), u is the electric potential (V), and e represents the amount of charge flowing into the closed surface (Q).

Boundary Condition: The boundary conditions play a crucial role in defining the behavior of the electric potential at the boundaries of the modeling domain. These conditions are described as follows:

$$\frac{\partial u}{\partial n} = 0, \text{ for } \in_0^s \tag{2.5}$$

$$\frac{\partial u}{\partial n} + \frac{cos(r,n)u}{r} = 0, \text{ for } \in_0^\infty \tag{2.6}$$

$$u1 = u2, \quad \text{for } \in_0 \tag{2.7}$$

Here, u represents the electric potential, $\in_0^s$ represents the boundary between the air and the formation, $\in_0^\infty$ represents the boundary at infinity, and $\in_0$ is the interface between two media. *n* indicates the outer normal direction of the boundary, and *r* is the distance from the point source to the boundary. These boundary conditions ensure the appropriate behaviour of the electric potential at different boundary interfaces within the modeling domain.

2.3.3 Mesh generation and refinement

Mesh generation and refinement are crucial steps in conducting 2D cross-well electrical resistivity tomography (ERT). Initially, the modeling domain is partitioned based on the layout of electrodes, which are often fixed as nodes. However, additional refinement is necessary to address the singular potential at the electrode positions.

Traditional approaches in ERT often utilize block-oriented grids for both finite difference (FD) and finite element (FE) calculations. These grids introduce grid lines between electrodes to minimize calculation errors. By adding two to four additional grid lines between electrodes, the relative error in calculations is typically reduced to around 4% for pole-pole configurations. However, for configurations with large geometric factors, such as dipole-dipole setups, further refinement is needed to reduce error amplification.

In 2D cross-well ERT, the use of unstructured meshes offers significant advantages. These meshes allow for refinement within specific regions, enabling fine meshing in areas with varying potential gradients near electrodes, while cell sizes grow towards the boundaries of the modeling domain.

Mesh refinement strategies can be categorized as a-posteriori or a-priori. In a-posteriori refinement, discretization depends on error estimation during the solution process. In contrast, a-priori refinement involves introducing information in advance, typically based on known critical regions. The a-priori approach is often preferred as it enables the enforcement of a locally fine mesh by adding supporting nodes during the mesh generation process.

a.)   b.)

Figure 2. 1 a.) Discretisation in Triangles:illustrates how the subsurface is divided into triangles, forming a mesh for modeling purposes. Each triangle represents a finite element used to approximate subsurface properties like resistivity distribution. This method allows for flexible mesh generation, particularly useful in complex geometries. b.) Mesh Refinement: highlights the process of mesh refinement, where additional detail is added to specific areas of the mesh. This enhancement aims to improve accuracy by capturing fine-scale features and variations in subsurface properties more precisely. Mesh refinement plays a crucial role in achieving higher resolution and fidelity in numerical simulations.

Chapter-3

Inversion and Model Resolution

3.1 Inversion

Cross-well Electrical Resistivity Tomography (ERT) inversion is a process employed to reconstruct the distribution of subsurface electrical resistivity or conductivity by analysing measurements obtained from electrodes placed in different wells. In the case of ERT, these measurements typically involve the apparent resistivity data.

Mathematically, the subsurface can be represented by a set of parameters, and the inversion process aims to estimate these parameters based on the recorded measurements. This computationally intensive process often results in a "recovered" or "constructed" model obtained through numerical techniques.

One critical step in ERT inversion is assessing whether the model adequately reproduces the observed measurements, ensuring that the misfit between observed and predicted data is minimized.

3.2 Inversion of Cross-well ERT Data

While cross-well ERT methods provide valuable information about subsurface resistivity or conductivity structures, they alone cannot directly infer the subsurface geology. To obtain an accurate spatial conductivity distribution, specific inversion algorithms and techniques are necessary. However, the inversion of cross-well ERT data poses challenges due to its under-determined nature and the potential presence of significant data errors, rendering the problem generally ill-posed.

Typically, inversion is carried out iteratively, with the process terminating when the root mean square error approaches a value close to zero. To perform the inversion, a parameter mesh is created to define the cells whose resistivities are to be determined. In this study, a triangular mesh is utilized, chosen based on computational considerations and requirements.
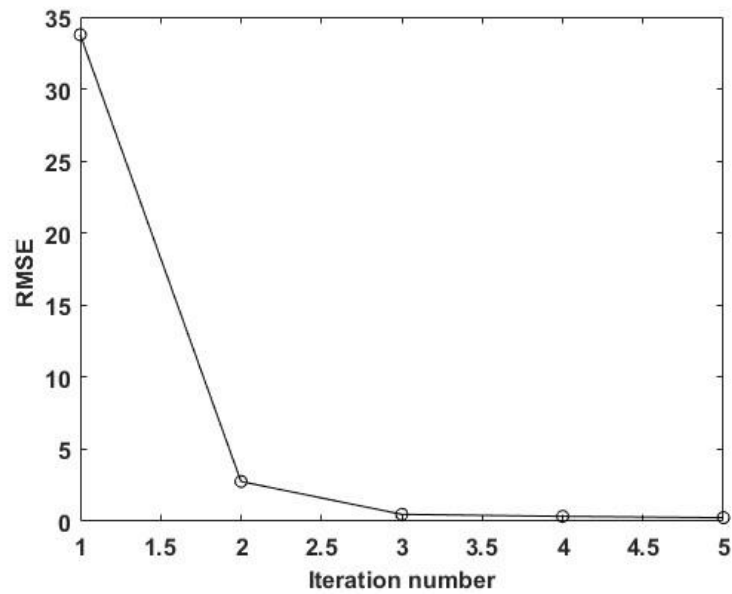
Figure 3. 1 depicts the convergence curve of data error plotted against the iteration number. This curve illustrates the iterative refinement process during geophysical inversion. At the start, with higher iteration numbers, the data error is large due to initial model parameter inaccuracies. However, as iterations progress, the data error decreases, indicating improved alignment between observed and modeled data as the inversion algorithm updates the model parameters
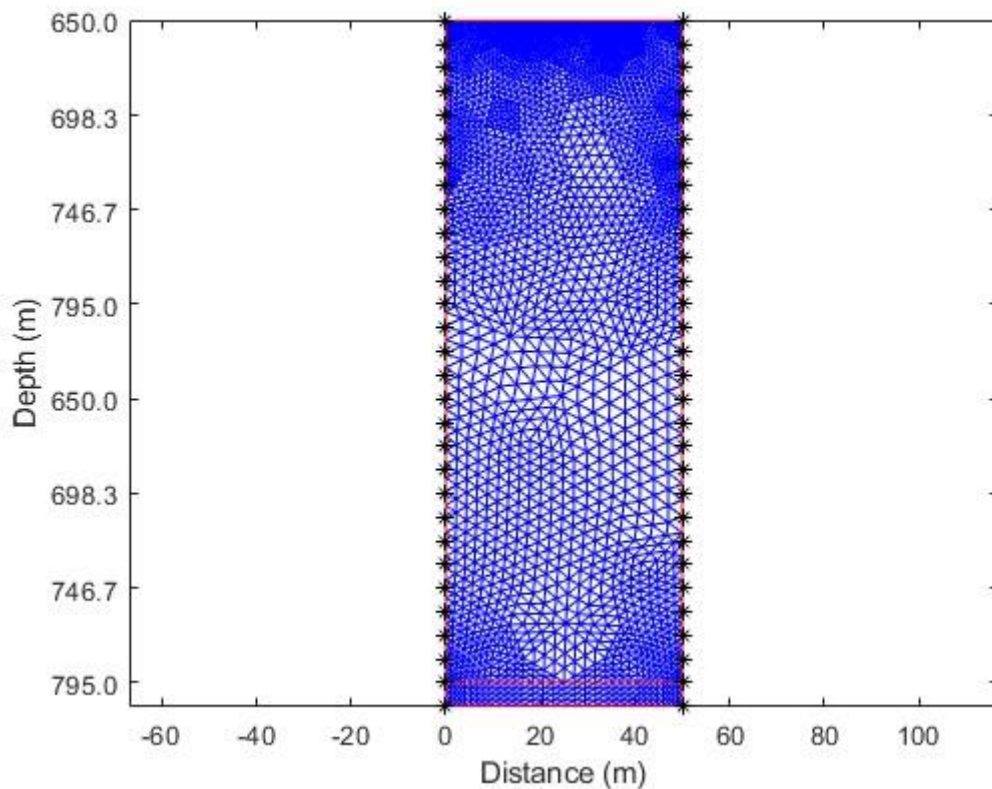
Figure 3. 2 Illustrates the iterative process of minimizing the Root Mean Square (RMS) error in geophysical inversion. The x-axis shows the iteration number, while the y-axis represents the RMS error. Initially, the RMS error is high due to initial parameter inaccuracies, but it decreases with each iteration as the inversion algorithm refines the model. Additionally, the plot may include a visualization of the triangular mesh grid used for inversion, dividing the subsurface into cells for analysis.

$$\|e\|_p^P = \sum_{j=1}^{N} |e_j|^P . \tag{3.1}$$

The norm proposed by (Ekblom and halan, 1987) which is a revised form of the l_p norm is used in this study. The expression for this norm is given below :-

$$l_p(e) = (e^2 + \varepsilon^2)^{P/2} \tag{3.2}$$

Here ε *is* a positive number. When ε is very small it will approach the l_p norm given in equation 1, for very large ε it behaves like a scaled sum of squares measure.

3.2.2 Minimization of Inverse Problem

We have taken p =2 since we are using L-2 Norm. The objective function for the minimization of data misfit along with function model regularization parameter and using Tikhonov parametric function in this study:

Considering s.t. $\phi < \phi^*$,

$$\phi^{\text{total}}(m) = \|W^d(F(m) - d^{\text{obs}})\|_2^2 + \lambda_1 \|\alpha_1 W_s^m(m - m^{\text{ref}})\|_2^2 \tag{3.3}$$

where ϕ^* is the target misfit. The first term corresponds to the data misfit and the second to model regularisation function with weighting matrices W^d and W_s^m .Using (Oldenburg and Ogobiri, 1998) the objective function to be minimized can be written as-

$$\phi = [\phi_d\{W^d(F(m) - d^{\text{obs}})\} - \phi^*] + \lambda_1[\phi_{m_1} \times \{\alpha_1 W_s^m(m - m^{\text{ref}})\}] \tag{3.4}$$

Let us assume that model at k th iteration is m^k, predicted data are d^k for this model and model update at k + 1 th iteration is $m^{k+1} = m^{k+1} - m^k$. Writing equation 2 for m^{k+1} using Taylor's series expansion of F(m) and discarding the second and higher order derivatives result in

$$\phi(m^{k+1}) = \left[\phi_d\left\{W^d\left(\left(F(m^k) + \frac{\partial F}{\partial m}\Delta m^{k+1}\right) - d^{obs}\right)\right\} - \phi^*\right]$$

$$+\lambda_1\left[\alpha_1\phi_{m_1}\left\{W_s^m\left(m^k + \Delta m^{k+1} - m^{ref}\right)\right\}\right] \tag{3.5}$$

Writing the sensitivity matrix $\frac{\partial F}{\partial m}$ as J^k —

$$\phi(m^{k+1}) = \left[\phi_d\left\{W^d\left(d^k + J^k\Delta m^{k+1} - d^{obs}\right)\right\} - \phi^*\right]$$

$$+\lambda_1\left[\alpha_1\phi_{m_1}\left\{W_s^m\left(m^k + \Delta m^{k+1} - m^{ref}\right)\right\}\right] \tag{3.6}$$

Now differentiating this equation w.r.t Δm^{k+1} and assuming ,

$$L_{j=(d,s)} = \begin{cases} W^d\left(d^k + J^k\Delta m^{k+1} - d^{obs}\right) \\ W_s^m\left(m^k + \Delta m^{k+1} - m^{ref}\right) \end{cases} \tag{3.7}$$

will lead to

$$\frac{\partial\phi}{\partial(\Delta m^{k+1})} = \left[\frac{\partial[\phi_d\{L_d\}-\phi^*]}{\partial(\Delta m^{k+1})} + \lambda_1\frac{\partial[\alpha_1\phi_{m_1}\{L_s\}]}{\partial(\Delta m^{k+1})}\right] \tag{3.8}$$

Differentiating the right side of equation 2.8 by the chain rule and putting the value of L_d and L_s from equation 2.7 result in

$$\frac{\partial[\phi_d\{L_d\}-\phi^*]}{\partial(\Delta m^{k+1})} = \frac{\partial\phi_d(L_d)}{\partial(L_d)}\frac{\partial\left(W^d(d^k+S^k\Delta m^{k+1}-d^{obs})\right)}{\partial(\Delta m^{k+1})} \, ,$$

$$\frac{\partial[\phi_d\{L_d\}-\phi^*]}{\partial(\Delta m^{k+1})} = \left(J^k\right)^T\left(W^d\right)^T\frac{\partial\phi_d(L_d)}{\partial(L_d)},$$

where superscript T is the transpose of the matrix. Similarly, putting the values of all the differential terms in equation 2.8 results in

$$\frac{\partial[\phi_d\{L_d\}-\phi^*]}{\partial(\Delta m^{k+1})} = \left(J^k\right)^T\left(W^d\right)^T\frac{\partial\phi_d(L_d)}{\partial(L_d)}, \tag{3.9}$$

Differential equation 2.2 with result in -

$$\frac{\partial\ell(e)}{\partial e} = p(e^2 + \varepsilon^2)^{\frac{p}{2}-1}e \tag{3.10}$$

Following the analogy of equation 2.10 and putting p=2 ,

$$\frac{\partial\phi_d(L_d)}{\partial(L_d)} = p((L_d)^2 + \varepsilon^2)^{\frac{p}{2}-1}(L_d) \tag{3.11}$$

$$\frac{\partial \phi_d(L_d)}{\partial (L_d)} = 2L_d \tag{3.12}$$

Similarly ,

$$\frac{\partial \phi_{m_1}(L_s)}{\partial (L_s)} = 2L_s \tag{3.13}$$

Now putting the values from equations 2.7, 2.12 and 2.13 in equation 2.9 and equating it to zero results in,

$$\left[\left(J^k\right)^T \left(W^d\right)^T R_d W^d \left(d^k + J^k \Delta m^{k+1} - d^{obs}\right) + \lambda_1 \left(\alpha_1 \left(W_s^m\right)^T R_s W_s^m \left(m^k + \Delta m^{k+1} - m^{ref}\right)\right)\right] = 0 \tag{3.14}$$

Simplifying for $(k+1)^{th}$ iteration,

$$\Delta m^{k+1} = \left[\left(J^k\right)^T \left(W^d\right)^T W^d J^k + \lambda_1 \alpha_1 \left(W_s^m\right)^T W_s^m\right]^{-1}$$

$$\times \left[\left(J^k\right)^T \left(W^d\right)^T W^d \left(d^{obs} - d^k\right) - \lambda_1 \left(\alpha_1 \left(W_s^m\right)^T W_s^m \left(m^k - m^{ref}\right)\right)\right] \tag{3.15}$$

In the equation above $\Delta m'^{(k+1)}$ represents the model update at the $(k+1)th$ iteration, calculated using the sensitivity matrix J^k, weighting matrices W^d and W_s^m, observed data d^{obs}, predicted data d^k, regularization parameter λ_1, Tikhonov parametric function parameter α_1, model at the kth iteration m^k, and reference model m^{ref}.

3.4 Cross Well ERT Inversion Workflow
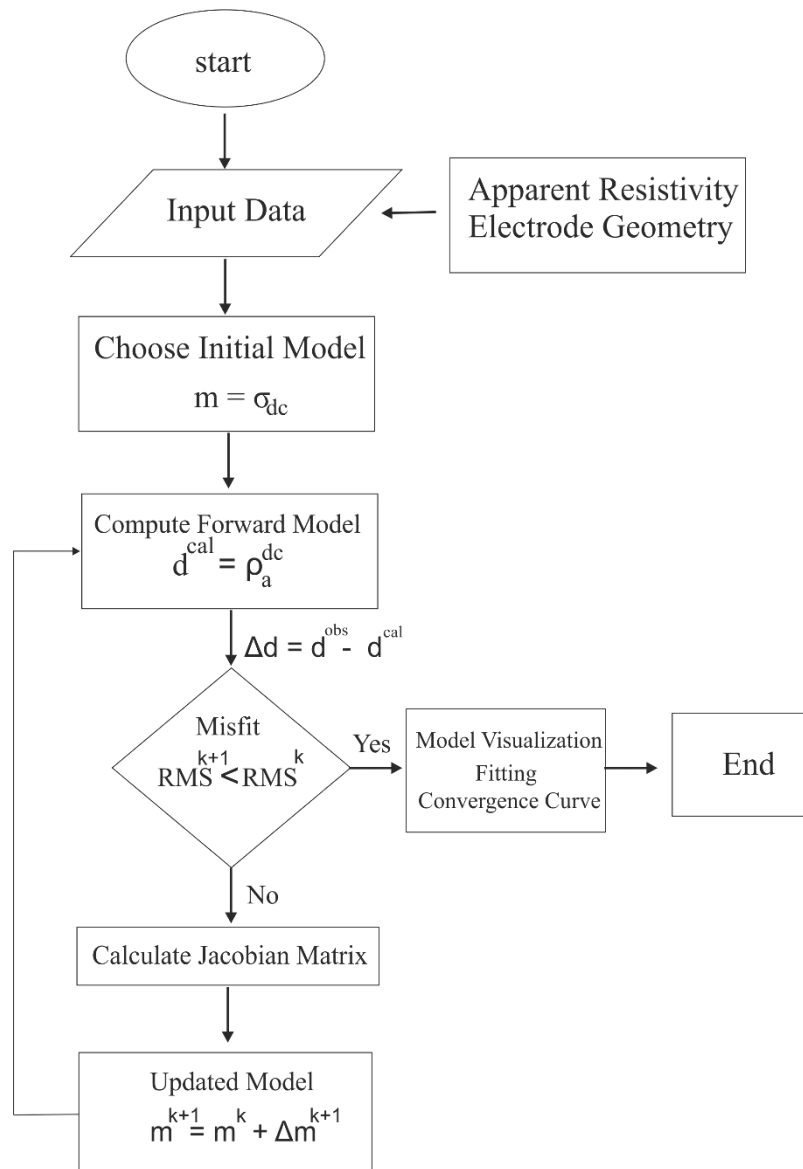
Figure 3. 3 depicts a concise flow chart detailing the sequential steps of the inversion procedure in geophysical modeling. It begins with data acquisition, followed by preprocessing to enhance data quality. Next, forward modeling predicts subsurface properties based on initial parameters. The inversion stage iteratively adjusts parameters to minimize discrepancies between observed and modeled data. Finally, the inverted model is evaluated and interpreted for subsurface insights.

3.5 Model Resolution Matrix

The model resolution matrix plays a crucial role in understanding the relationship between the estimated model and the true model in inverse problems. Essentially, it quantifies how accurately the estimated model represents the true model.

$$m^{est.} = G^{-g} d^{true} \tag{3.16}$$

$$m^{est.} = G^{-g} G m^{true} \tag{3.17}$$

$$m^{est.} = R m^{true} \tag{3.18}$$

Given equations (3.16) and (3.17) from the context, where $m^{est.}$ represents the estimated model, m^{true} represents the true model, and G is the data kernel or forward model matrix, we derive the expression for the model resolution matrix $R=G^{-g}G$ as in equation (3.18). For the case of under-determined problem as in the case of DC resistivity problems, the generalised inverse can be written as –

$$G^{-g} = G^T (GG^T)^{-1} \tag{3.19}$$

Using Eq 3.17 , we can write model resolution matrix R as,

$$R = G^T (GG^T)^{-1} G \tag{3.20}$$

Considering J as (N*M) Jacobian Matrix and C as (M*M) smoothing matrix, we can rewrite the model resolution matrix R as follows (Menke, 1989)

$$R = (J^T w_d^T w_d A + \alpha C^T C)^{-1} A^T w_d^T w_d J$$

In the equation above, R represents the model resolution matrix, J is the ($N{\times}M$) Jacobian matrix, C denotes the ($M{\times}M$) smoothing matrix, w_d stands for the weighting matrix for data, A signifies the data misfit matrix or observation operator, and α is the regularization parameter.

3.6 Model Resolution Analysis

The model resolution matrix, denoted as R, serves as a tool for evaluating the quality of a model's resolution (e.g., as discussed by Alumbaugh et al., 2000, and by (Candansayar and M.E., 2008)). By examining the diagonal elements of this matrix, we can establish a parameter indicating the level of resolution achieved by the data. Additionally, the Dirichlet Spread Function comes into play to quantify the disparity between the actual model resolution matrix R and an ideal resolution matrix, typically represented as an identity matrix.

We have considered different synthetic model to analysis the model resolution

Chapter 4

Result and Conclusions

In this chapter, we present the outcomes of the inversion process and the analysis of model resolution discussed in Chapter 3. The results provide insights into the effectiveness of the cross-well Electrical Resistivity Tomography (ERT) method in characterizing subsurface properties and detecting anomalies such as CO2 injection.

4.1 Inversion Results

The inversion results provide crucial insights into the spatial distribution of subsurface electrical resistivity or conductivity, offering a detailed view of the underground structures and fluid dynamics. Here, we analyze two synthetic models first one is homogeneous and the second one is heterogeneous and we make these models like we are injecting the CO_2 into the subsurface.

4.1.1 Model 1

In our study, we employed a synthetic model representing a homogeneous medium with a resistivity of 200 ohm-m. To simulate the presence of CO2, we introduced a body with a resistivity of 100 ohm-m into this medium. The body is defined by a polygonal shape with vertices at coordinates 15, 16, 17, 26, 27, and 28.

Our objective was to mimic CO2 injection from a well, with the gradual spread of CO2 within the subsurface medium. To achieve this, we incrementally adjusted the size or extent of the body at different time intervals, representing the progression of CO2 injection.

At time $t1$, the vertices defining the body were located at coordinates 15, 16, 17, 26, 27, and 28 with the resistivity of the medium remaining at 100 ohm-m and the resistivity of the body was 10 ohm-m.

At time $t2$, the vertices shifted to coordinates 12, 13, 14, 30, 31, and 32, with the resistivity of the medium remaining at 100 ohm-m and the resistivity of the body adjusted to 15.85 ohm-m.

At time $t3$, the vertices further changed to coordinates 10, 11, 12, 34, 35, and 36, while the resistivity of the medium remained constant at 100 ohm-m, and the resistivity of the body increased to 25.12 ohm-m.

Finally, at time $t4$, the vertices shifted to coordinates 10, 11, 12, 35, 36, and 37, with the resistivity of the medium staying at 100 ohm-m, and the resistivity of the body increasing to 39.81 ohm-m.

These adjustments represent the dynamic nature of CO2 injection and spread within the subsurface medium over time, allowing us to study its impact and behavior in a controlled environment.
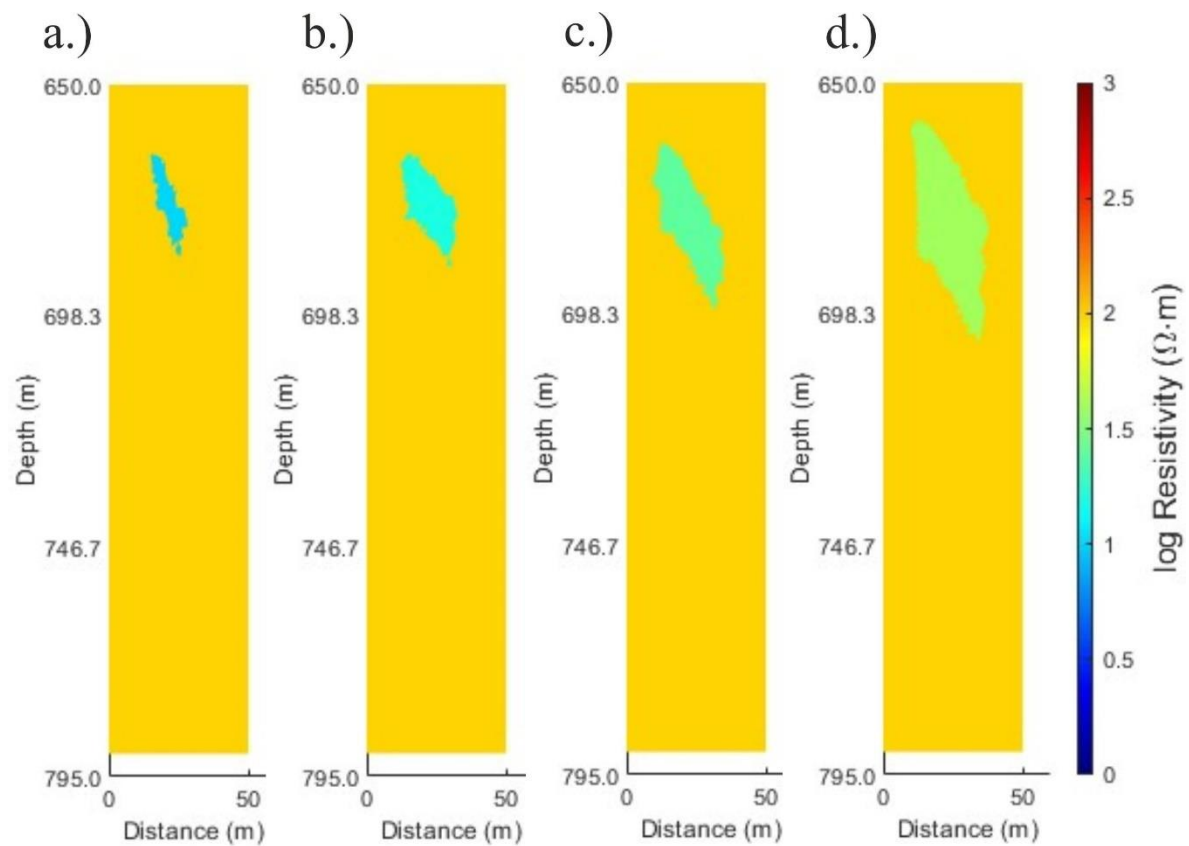
Figure 4. 1 Simulation of CO2 injection and spread within a homogeneous subsurface medium. The polygon represents the injected CO2 body, with changing resistivity values over time (t1-t4). The coordinates of the body's vertices and the resistivity of the medium and body are detailed at each time step. This dynamic model provides insights into the behavior and impact of CO2 injection in a controlled environment
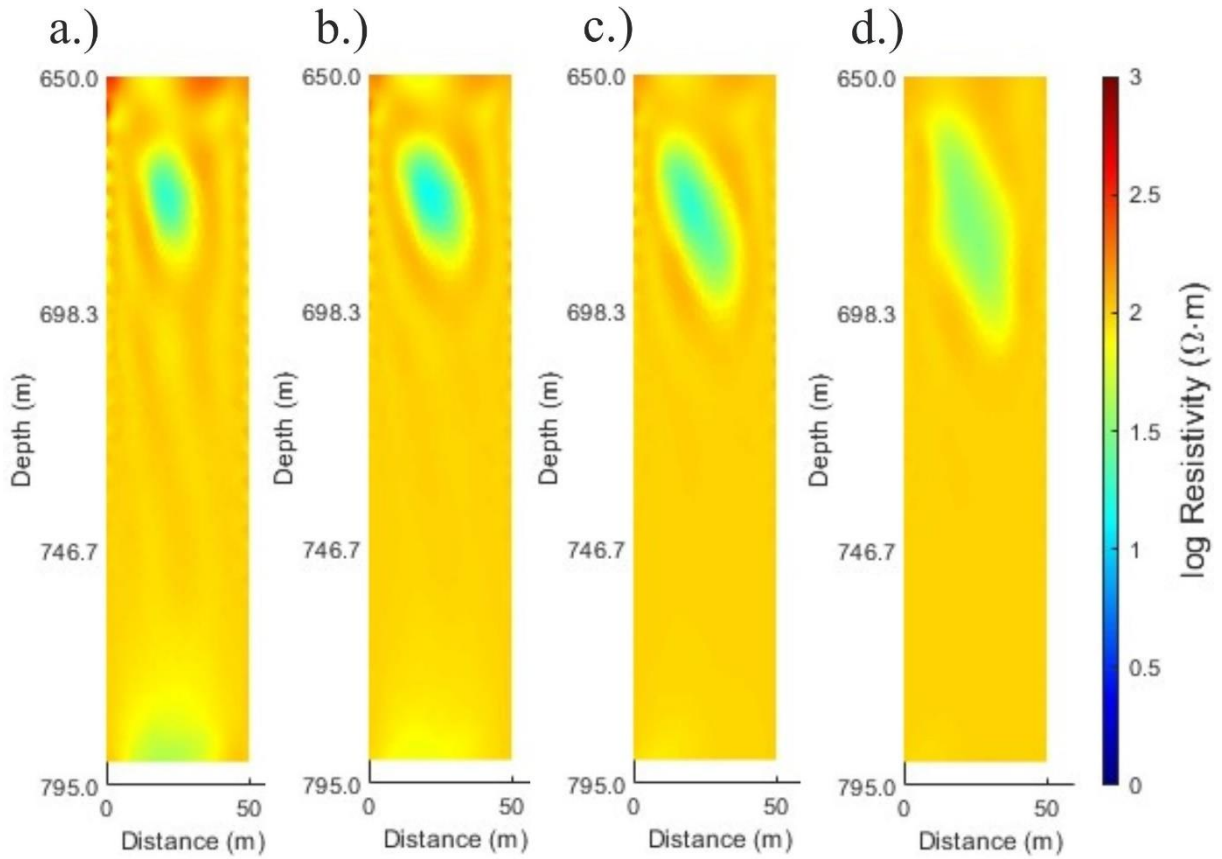
Figure 4. 2 Inverse modeling results show the inferred CO2 distribution over time (t1-t4), along with the evolving resistivity values of the injected CO2 body. This visualization provides valuable insights into the spatial distribution and dynamic behavior of injected CO2 within the subsurface medium

Homogeneous Subsurface Medium

In Figure 4.1, we observe the simulation of CO2 injection and spread within a homogeneous subsurface medium. The inverted electrical resistivity imaging model (Figure 4.2) captures the temporal evolution of the injected CO2 body, demonstrating the technique's ability to track fluid migration processes accurately. The consistency between the simulated and inverted models indicates the effectiveness of the inversion process in reconstructing subsurface resistivity distributions in homogeneous environments.

4.1.2 Model 2

In our study, we utilized a synthetic model representing a heterogeneous medium with varying resistivity values. At t1, the resistivity values of the medium were as follows: the first layer had a resistivity of approximately 125.89 ohm-m, the second layer had a resistivity of approximately 125.89 ohm-m, and the resistivities of the third and fourth layers were 100 ohm-m and 100 ohm-m, respectively.

To simulate CO_2 injection and spread within this heterogeneous medium, we introduced a body with a resistivity of 10 ohm-m. The body was defined by a polygonal shape with vertices at coordinates 15, 16, 17, 26, 27, and 28.

At $t2$, the vertices shifted to coordinates 12, 13, 14, 30, 31, and 32. The resistivity values of the medium were updated to approximately 158.49 ohm-m for the first layer, 158.49 ohm-m for the second layer, and remained constant at 100 ohm-m for the third and fourth layers. The resistivity of the body was adjusted to 6.3095 ohm-m.

At $t3$, the vertices shifted to coordinates 10,11,12,34,35 and 36. The resistivity values of the medium were updated to approximately 199.53 ohm-m for the first layer, 199.53199.53 ohm-m for the second layer, and remained constant at 100 ohm-m for the third and fourth layers. The resistivity of the body was adjusted to approximately 6.3095 ohm-m.

At $t4$, the vertices shifted to coordinates 10,11,12,34,35 and 36. The resistivity values of the medium were updated to approximately 223.87 ohm-m for the first layer, 223.87223.87 ohm-m for the second layer, and remained constant at 100100 ohm-m for the third and fourth layers. The resistivity of the body was adjusted to approximately 4.4668 ohm-m.
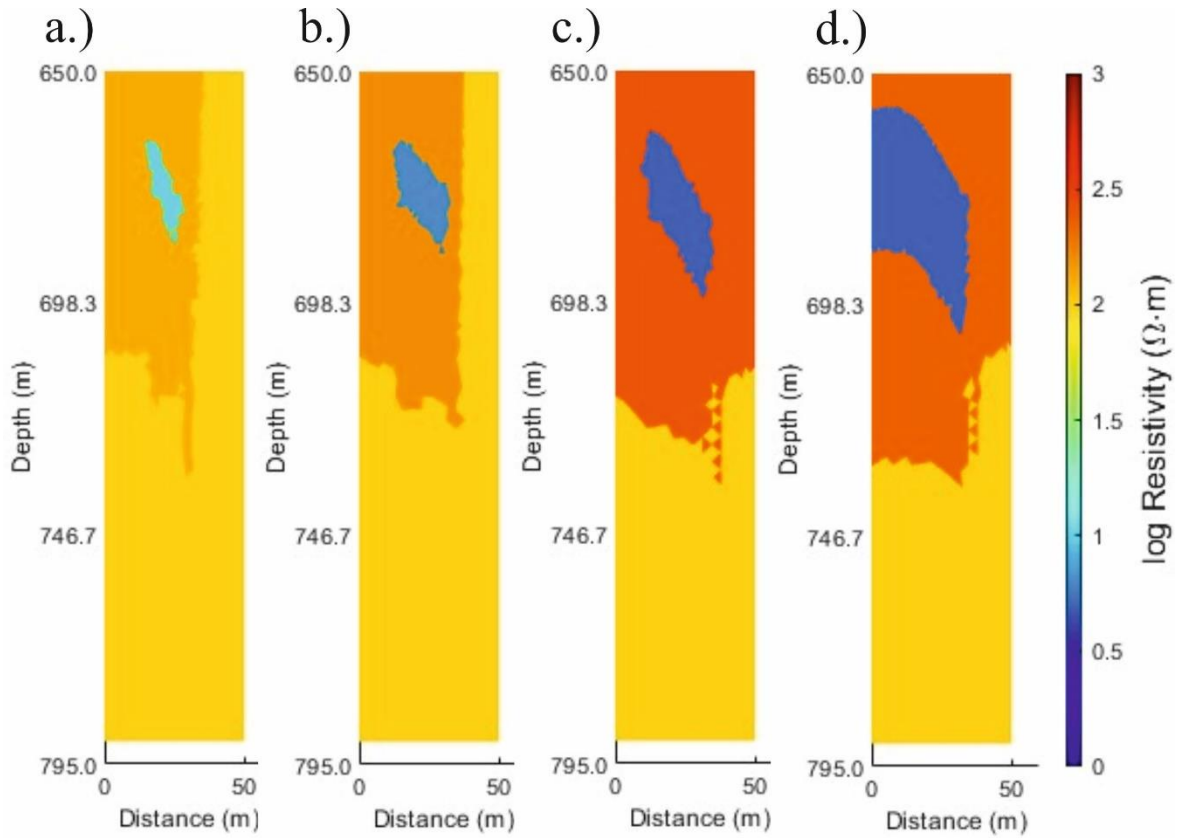
Figure 4. 3 Simulation of CO2 injection and spread within a heterogeneous subsurface. The polygon represents injected CO2, with changing resistivity over time (t1-t4). Varying colors indicate the heterogeneous nature of the subsurface. Insights gained from this model aid in understanding CO2 behaviour in realistic geological settings
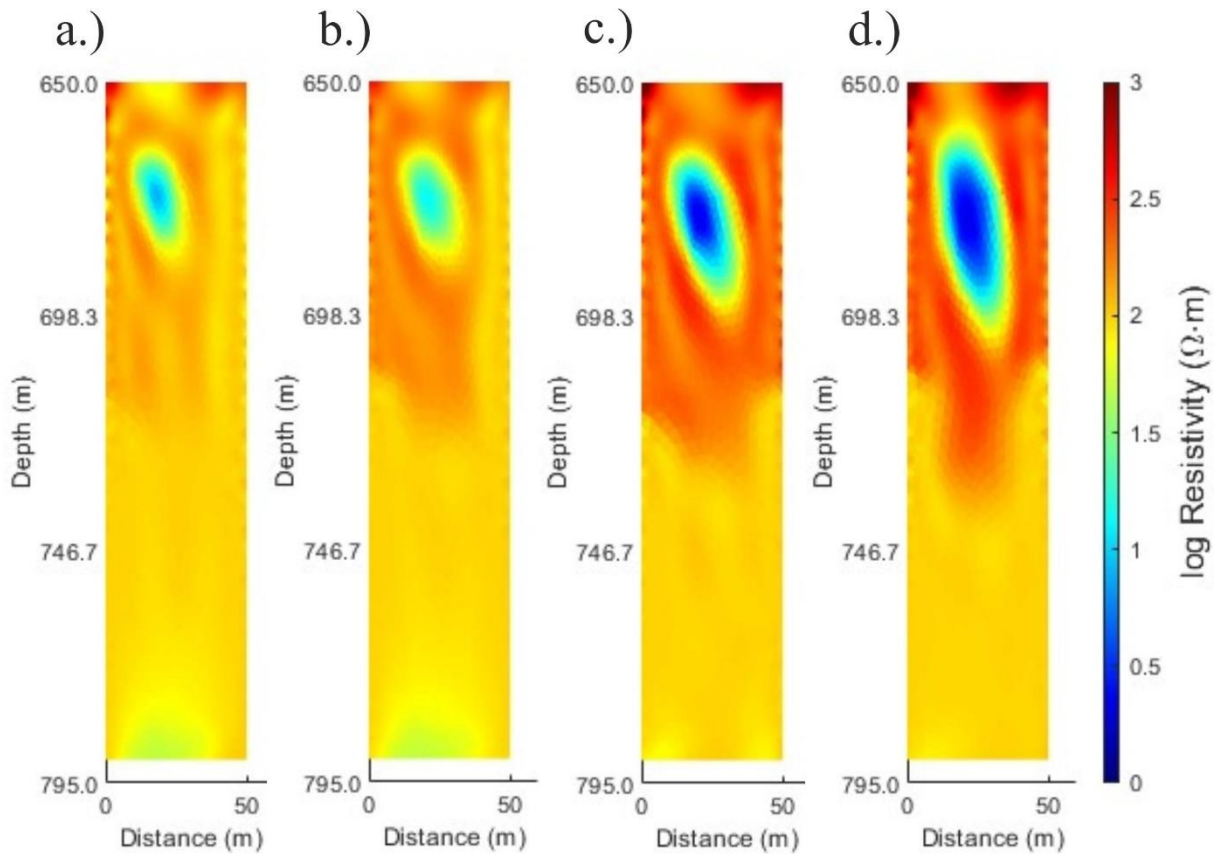
Figure 4. 4 Inverse modeling of CO2 injection and propagation within a heterogeneous subsurface medium. The inverted results depict the inferred spatial distribution of CO2 over time (t1-t4), considering the dynamic changes in resistivity associated with the injected CO2 body. The diverse colors reflect the heterogeneity of the subsurface, providing valuable insights into CO2 behavior within realistic geological formations.

Heterogeneous Subsurface Structures

Figure 4.3 illustrates the simulation of CO2 injection and spread within a heterogeneous subsurface, presenting additional challenges for subsurface imaging. Despite the complexity introduced by heterogeneities, the inverted electrical resistivity imaging model (Figure 4.4) successfully delineates the spatial distribution of injected CO2 and captures dynamic changes in subsurface resistivity. The diverse colors in the inverted model reflect the heterogeneity of the subsurface, providing valuable insights into fluid migration behavior in realistic geological settings.

4.1.3 Analysis of Inversion Results

The comparison between simulated and inverted models reveals several important findings:

- **Resolution of Subsurface Features**: The inversion process effectively resolves subsurface features, including fluid plumes and geological structures, even in heterogeneous environments. This capability is crucial for applications such as environmental monitoring and resource management.

- **Quantification of Fluid Dynamics**: The inverted models offer quantitative information about fluid dynamics, enabling the assessment of fluid migration rates and pathways. This information enhances our understanding of subsurface processes and aids in contamination remediation efforts.

- **Characterization of Geological Structures:** The inversion results provide insights into subsurface geological structures, facilitating geological mapping and hydrogeological studies. Accurate delineation of these structures improves our understanding of subsurface properties and behavior.

4.2 Model Resolution Analysis: Evaluating Resolution Quality

The model resolution analysis, based on the resolution matrix denoted as R, serves as a critical tool for assessing the quality of resolution achieved by the inversion process (e.g., as discussed by (Alumbaugh, 2000), and by (Candansayar, 2008)). By examining the diagonal elements of this matrix, we can quantify the level of resolution attained by the inversion model, providing valuable insights into its effectiveness in capturing subsurface features.

4.2.1 Synthetic Model 1

For the cross-well synthetic data analysis, a single-layer model was considered with the following resistivity values:

Background medium: $\rho_1 = 100$ $\Omega \cdot$m

Anomalous body: $\rho_2 = 10$ $\Omega \cdot$m

Figure 4. 5 Cross-Well Synthetic Data Analysis: Considering a single layer model with the resistivity values of $\rho_1 = 100$ $\Omega{\cdot}m$ for the background medium and $\rho_2 = 10$ $\Omega{\cdot}m$ for the anomalous body:(a) Synthetic two-layer model at time t_1, with the vertices defining the body located at coordinates 15, 16, 17, 26, 27, and 28 while maintaining the resistivity of the medium at 100 $\Omega{\cdot}m$ and the resistivity of the body at 10 $\Omega{\cdot}m$.(b) Inverted electrical resistivity imaging model based on the synthetic data.(c) Model Resolution Matrix depicting the resolution quality of the inverted model.

4.2.2 Synthetic Model 2

For the cross-well synthetic data analysis, a single-layer model was considered with the following resistivity values:

Background medium: $\rho_1 = 100\ \Omega\cdot m$

Anomalous body: $\rho_2 = 15.85\ \Omega\cdot m$
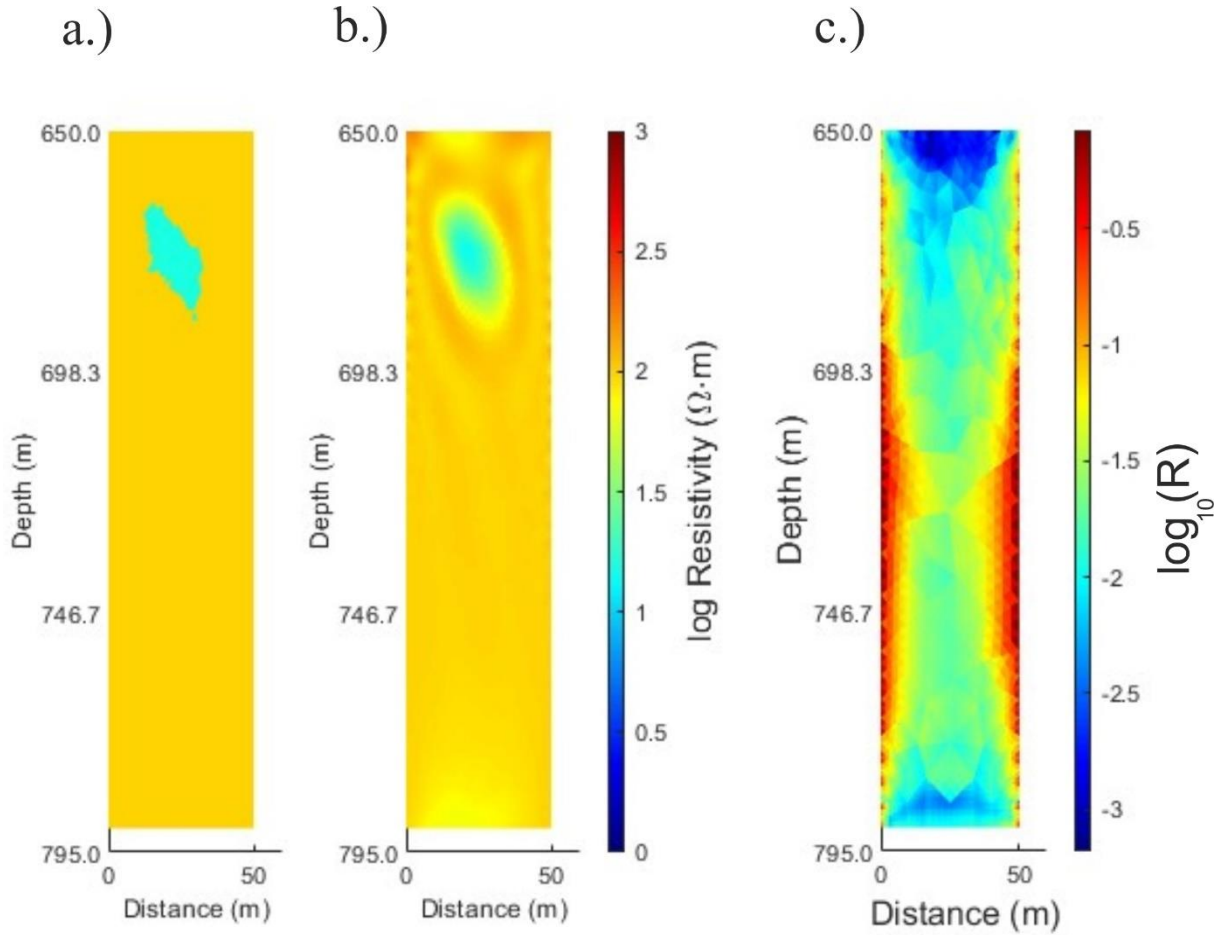
Figure 4. 6 Cross-Well Synthetic Data Analysis: (a) Synthetic two-layer model at time t_2, with the vertices defining the body shifted to coordinates 12, 13, 14, 30, 31, and 32 while maintaining the resistivity of the medium at 100 $\Omega\cdot m$ and adjusting the resistivity of the body to 15.85 $\Omega\cdot m$.(b) Inverted electrical resistivity imaging model based on the synthetic data.(c) Model Resolution Matrix depicting the resolution quality of the inverted model.

4.2.3 Synthetic Model 3

For the cross-well synthetic data analysis, a single-layer model was considered with the following resistivity values:

Background medium: $\rho_1 = 100$ $\Omega \cdot m$

Anomalous body: $\rho_2 = 25.12$ $\Omega \cdot m$
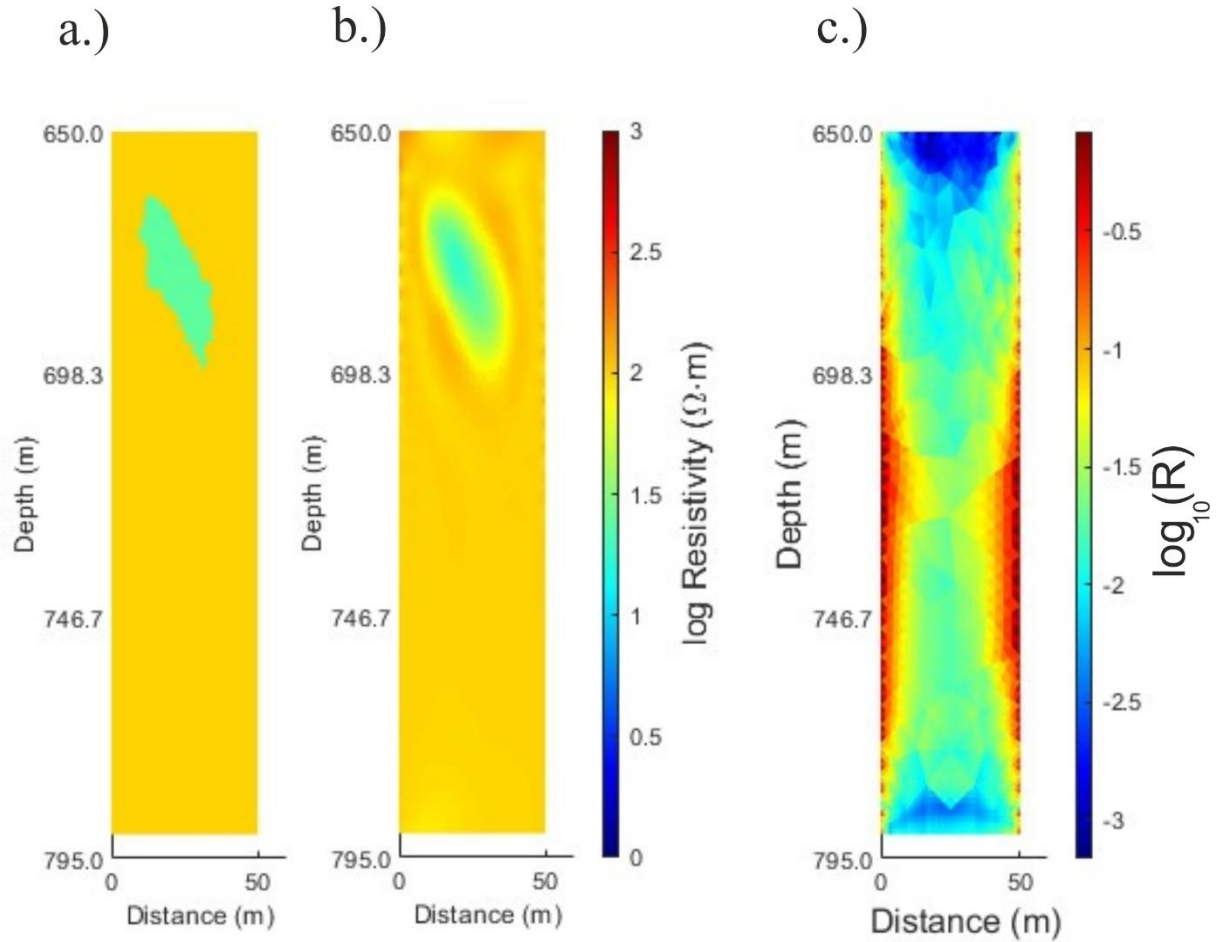
Figure 4. 7 Cross-Well Synthetic Data Analysis: (a) Synthetic two-layer model at time t_2, with the vertices defining the body shifted to coordinates 10, 11, 12, 34, 35, and 36 while maintaining the resistivity of the medium at 100 $\Omega \cdot m$ and adjusting the resistivity of the body to 25.12 $\Omega \cdot m$.(b) Inverted electrical resistivity imaging model based on the synthetic data.(c) Model Resolution Matrix depicting the resolution quality of the inverted model.

4.2.4 Synthetic Model 4

For the cross-well synthetic data analysis, a single-layer model was considered with the following resistivity values:

Background medium: $\rho_1 = 100\ \Omega\cdot m$

Anomalous body: $\rho_2 = 39.81\ \Omega\cdot m$
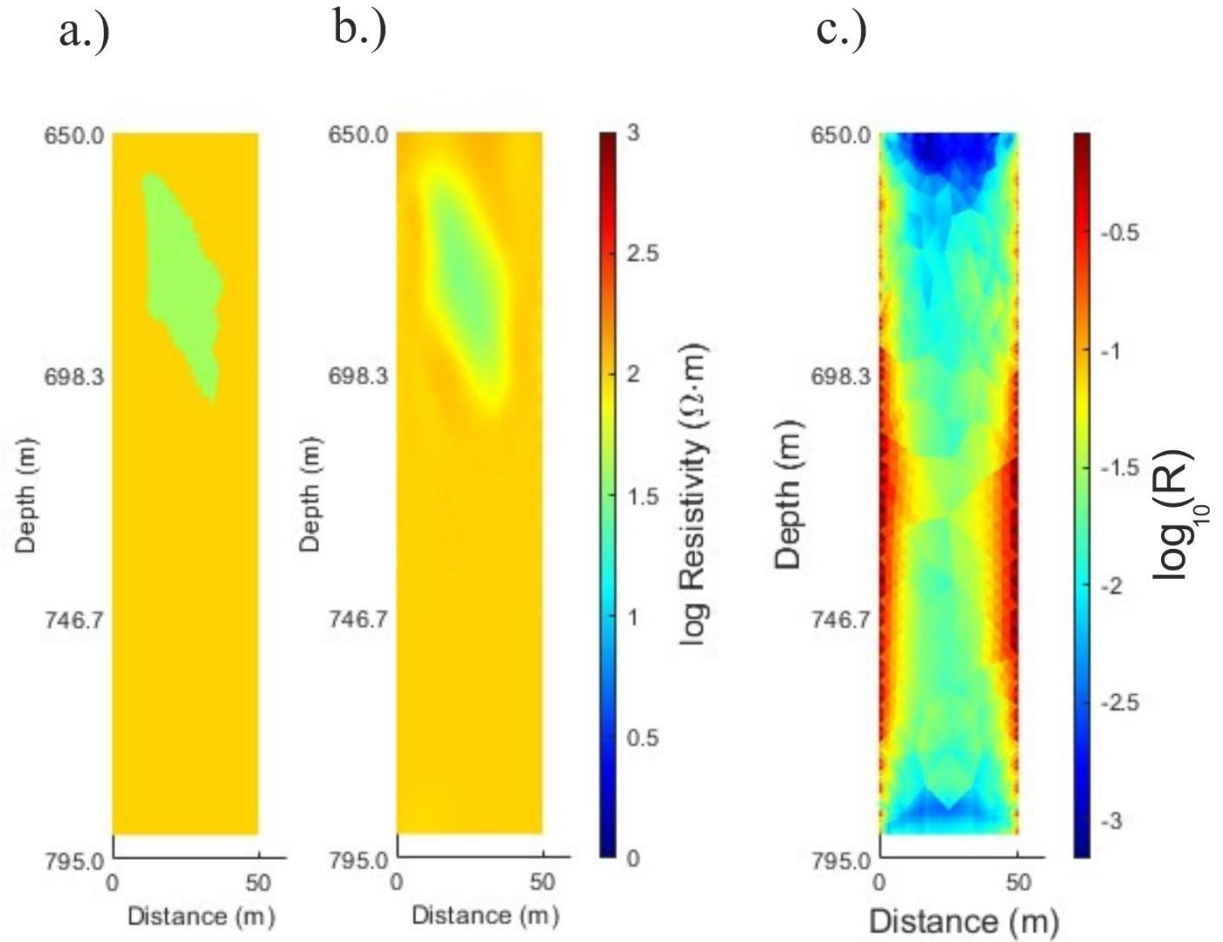
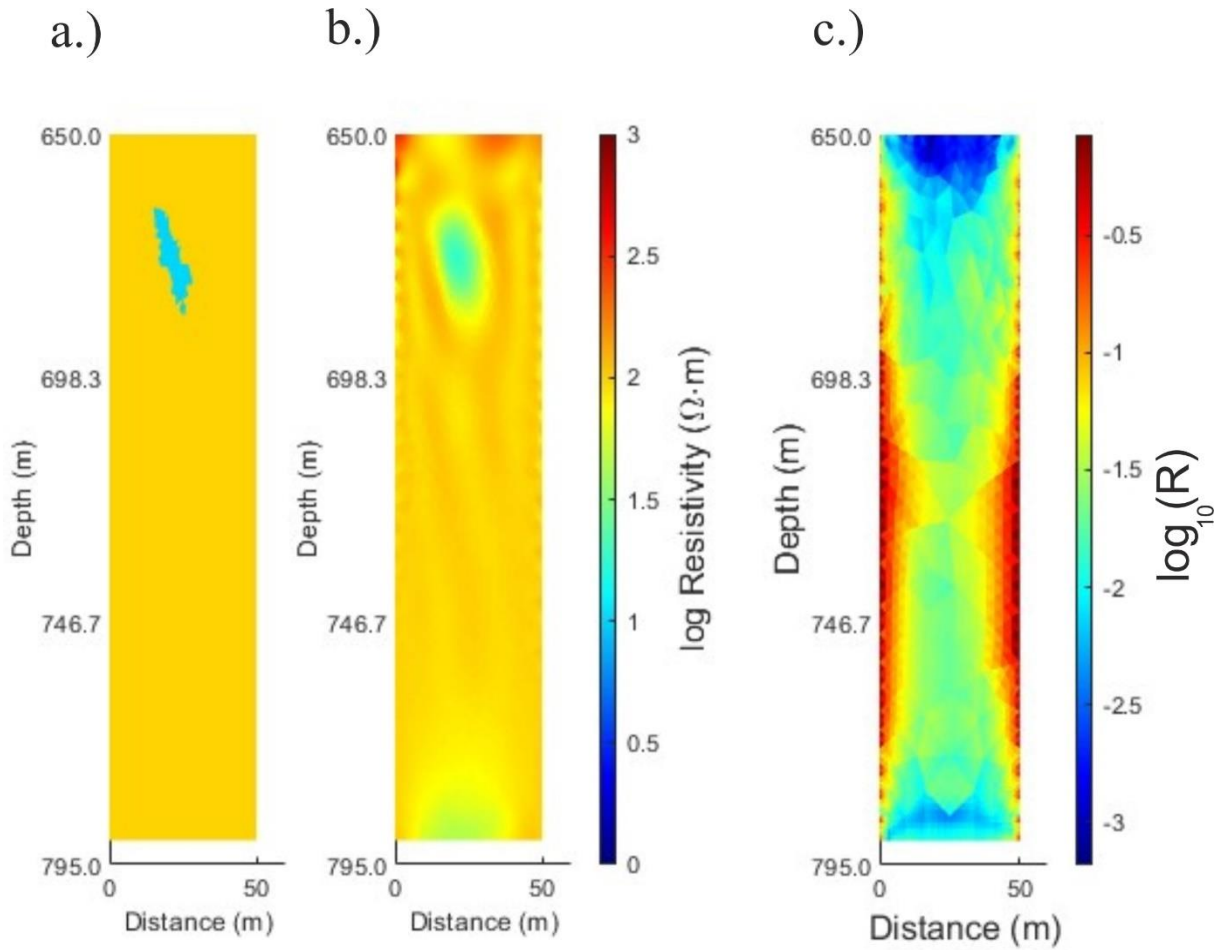*Figure 4. 8 Cross-Well Synthetic Data Analysis: (a) Synthetic two-layer model at time t_2, with the vertices defining the body shifted to coordinates 10, 11, 12, 35, 36, and 37 while maintaining the resistivity of the medium at 100 $\Omega\cdot m$ and adjusting the resistivity of the body to 39.81 $\Omega\cdot m$.(b) Inverted electrical resistivity imaging model [Ohm·m] based on the synthetic data.(c) Model Resolution Matrix depicting the resolution quality of the inverted model.*

4.2.5 Synthetic Model 5

We utilized a synthetic model representing a heterogeneous medium with varying resistivity values. At $t1$, the resistivity values of the medium were as follows: the first layer had a resistivity of approximately 125.89 ohm-m, the second layer had a resistivity of approximately 125.89 ohm-m, and the resistivities of the third and fourth layers were 100 ohm-m and 100 ohm-m, respectively.To simulate CO_2 injection and spread within this heterogeneous medium, we introduced a body with a resistivity of 10 ohm-m. The body was defined by a polygonal shape with vertices at coordinates 15, 16, 17, 26, 27, and 28.

Figure 4. 9 (a)Synthetic model representing a heterogeneous medium characterized by diverse resistivity values. Initially, at time t1, the resistivity values of the layers were as follows: approximately 125.89 ohm-m for both the first and second layers, while the third and fourth layers exhibited resistivities of 100 ohm-m each. .(b) Inverted electrical resistivity imaging model [Ohm·m] based on the synthetic data.(c) Model Resolution Matrix depicting the resolution quality of the inverted model.

4.2.6 Synthetic Model 6

We utilized a synthetic model representing a heterogeneous medium with varying resistivity values. At t1, the resistivity values of the medium were as follows: the first layer had a resistivity of approximately 158.49 ohm-m, the second layer had a resistivity of approximately 158.49 ohm-m, and the resistivities of the third and fourth layers were 100 ohm-m and 100 ohm-m, respectively. To simulate CO_2 injection and spread within this heterogeneous medium, we introduced a body with a resistivity of 6.3095 ohm-m. The body was defined by a polygonal shape with vertices at coordinates 12, 13, 14, 30, 31, and 32.

Figure 4. 10 (a) Synthetic model representing a heterogeneous medium characterized by diverse resistivity values. Initially, at time t1, the resistivity values of the layers were as follows: approximately 158.49 ohm-m for both the first and second layers, while the third and fourth layers exhibited resistivities of 100 ohm-m each. .(b) Inverted electrical resistivity imaging model [Ohm·m] based on the synthetic data.(c) Model Resolution Matrix depicting the resolution quality of the inverted model.

4.2.7 Synthetic Model 7

We utilized a synthetic model representing a heterogeneous medium with varying resistivity values. At t1, the resistivity values of the medium were as follows: the first layer had a resistivity of approximately 199.53199.53 ohm-m, the second layer had a resistivity of approximately 199.53199.53 ohm-m, and the resistivities of the third and fourth layers were 100 ohm-m and 100 ohm-m, respectively. To simulate CO_2 injection and spread within this heterogeneous medium, we introduced a body with a resistivity of 5.623 ohm-m. The body was defined by a polygonal shape with vertices at coordinates 10,11,12,34,35 and 36.
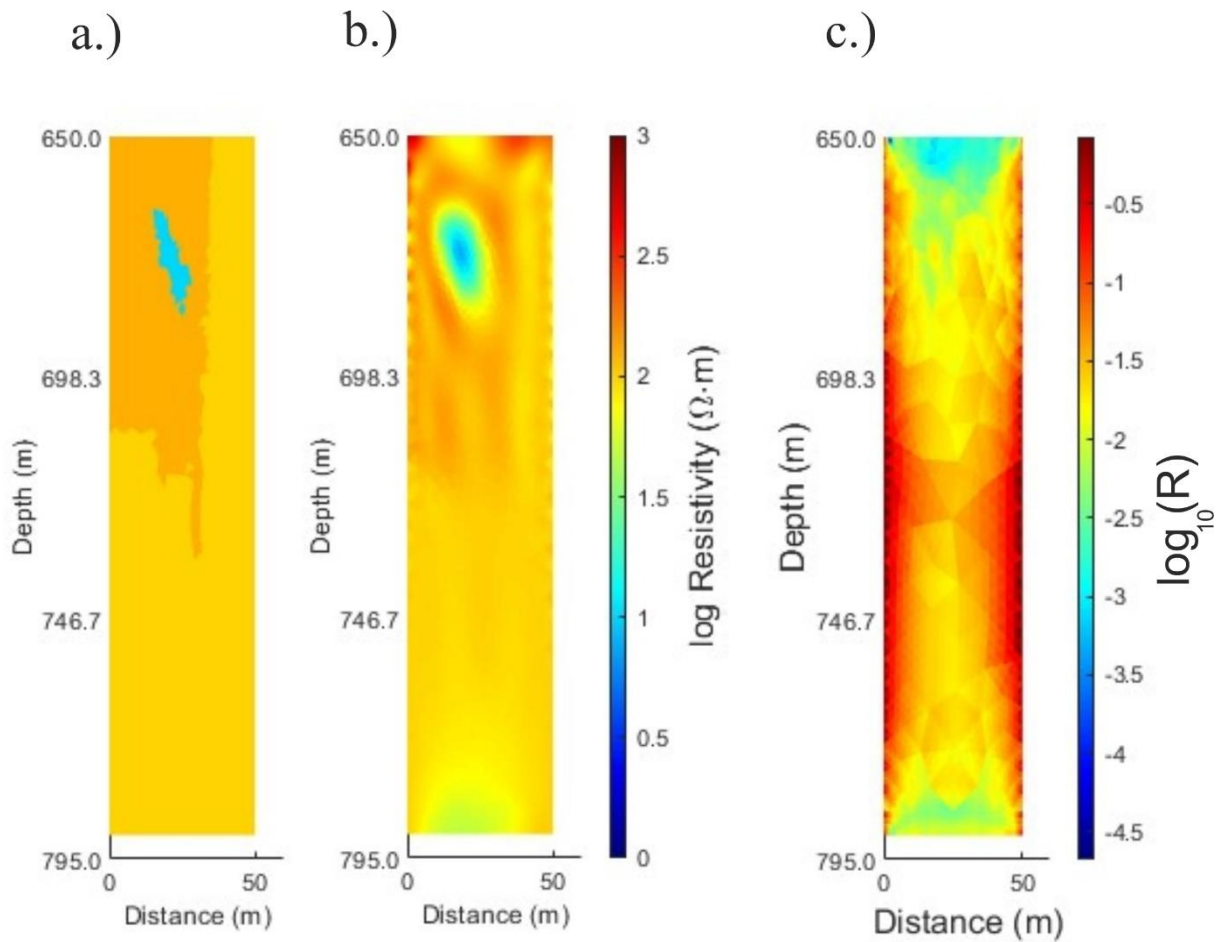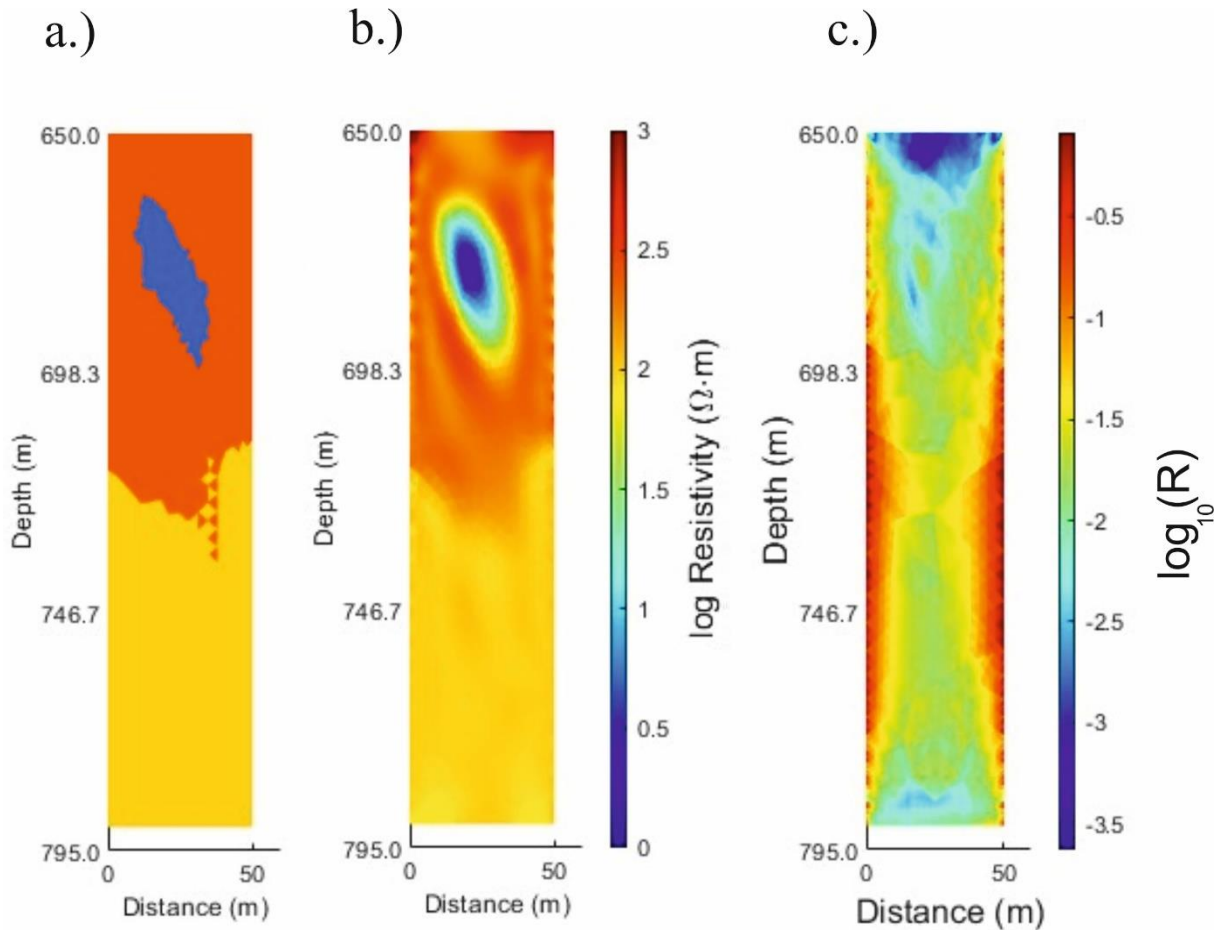

Figure 4. 11 (a) Synthetic model representing a heterogeneous medium characterized by diverse resistivity values. Initially, at time t1, the resistivity values of the layers were as follows: approximately 199.53199.53 ohm-m for both the first and second layers, while the third and fourth layers exhibited resistivities of 100 ohm-m each. .(b) Inverted electrical resistivity imaging model [Ohm·m] based on the synthetic data.(c) Model Resolution Matrix depicting the resolution quality of the inverted model.

4.2.8 Synthetic Model 8

      We utilized a synthetic model representing a heterogeneous medium with varying resistivity values. At t1, the resistivity values of the medium were as follows: the first layer had a resistivity of approximately 223.87223.87 ohm-m, the second layer had a resistivity of approximately 223.87223.87 ohm-m, and the resistivities of the third and fourth layers were 100 ohm-m and 100 ohm-m, respectively.To simulate CO_2 injection and spread within this heterogeneous medium, we introduced a body with a resistivity of 4.4668 ohm-m. The body was defined by a polygonal shape with vertices at coordinates 10,11,12,34,35 and 36.
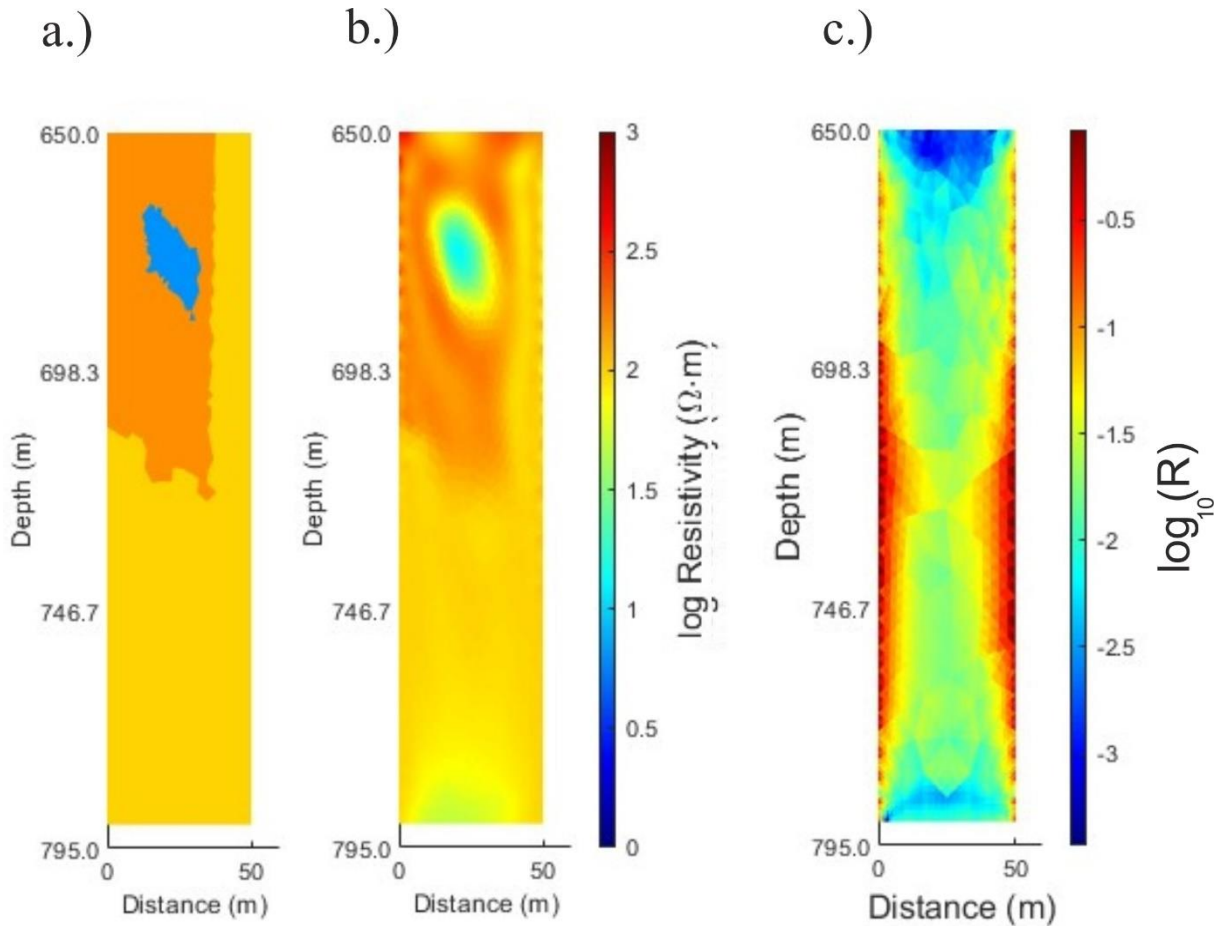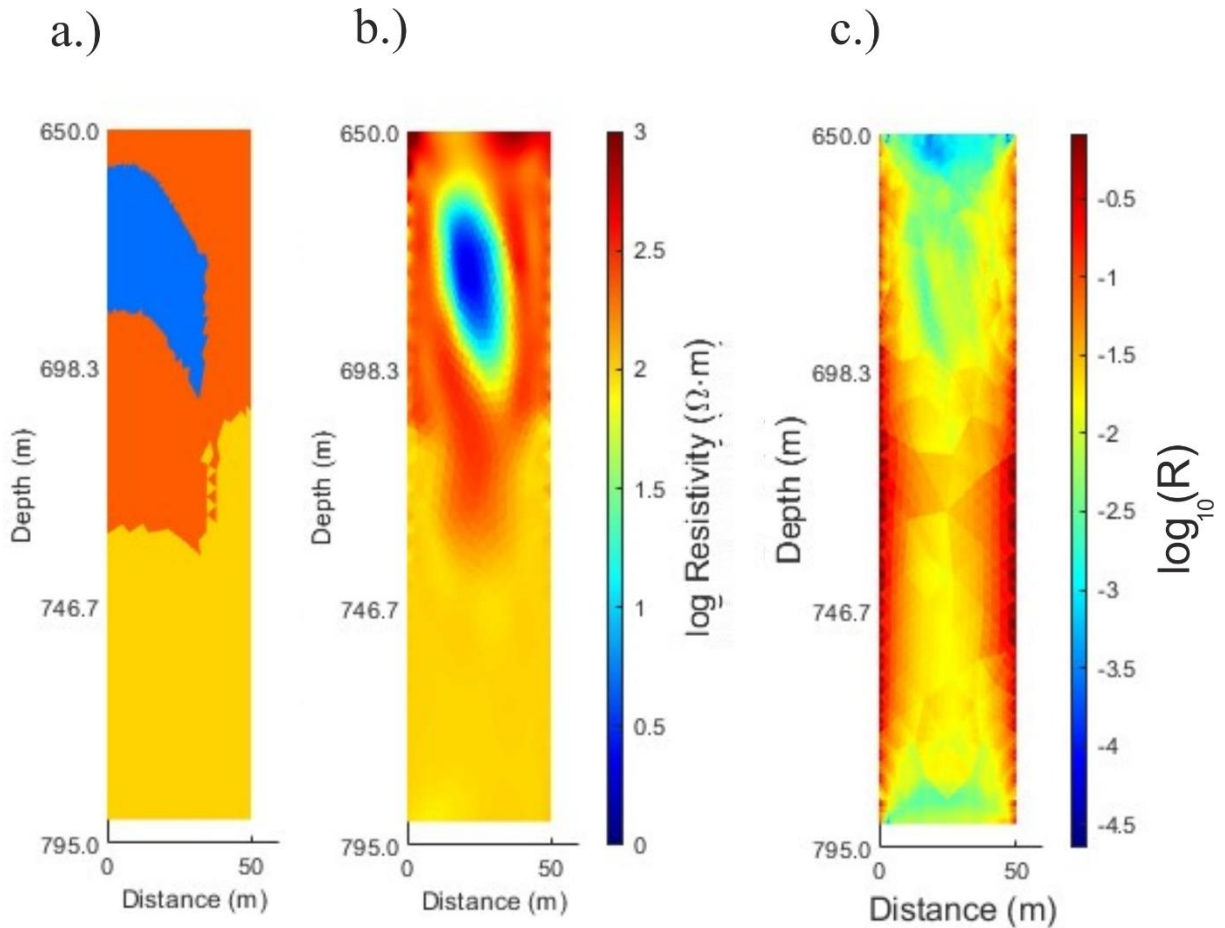

Figure 4. 12 (a) Synthetic model representing a heterogeneous medium characterized by diverse resistivity values. Initially, at time t1, the resistivity values of the layers were as follows: approximately 223.87223.87 ohm-m for both the first and second layers, while the third and fourth layers exhibited resistivities of 100 ohm-m each. .(b) Inverted electrical resistivity imaging model [Ohm·m] based on the synthetic data.(c) Model Resolution Matrix depicting the resolution quality of the inverted model.

4.2.9 Analysis of Model Resolution

Across the synthetic models analyzed, we observed variations in the resolution quality, as indicated by the Model Resolution Matrices. The diagonal elements of these matrices provide a measure of the resolution achieved for each model configuration, with higher values indicating better resolution. By comparing the resolution matrices across different scenarios, considering the variable background resistivity, we can identify optimal conditions for imaging subsurface anomalies and assess the impact of varying resistivity contrasts on resolution quality.

4.2.9 Implications for Subsurface Imaging

The analysis of model resolution provides valuable insights into the capabilities and limitations of the inversion technique in imaging subsurface structures. By understanding the factors influencing resolution quality, such as resistivity distribution and contrast, researchers and practitioners can optimize data acquisition and processing strategies to enhance imaging performance. Additionally, insights gained from model resolution analysis contribute to the development of advanced inversion methodologies tailored to specific geological settings and exploration objectives.

Chapter 5

Conclusions

The study delves into the intricate process of Cross-well Electrical Resistivity Tomography (ERT) inversion and its significance in reconstructing subsurface electrical resistivity or conductivity distributions. By analysing measurements obtained from electrodes placed in different wells, ERT inversion aims to estimate subsurface parameters, often resulting in a "recovered" or "constructed" model through numerical techniques.

Throughout the study, the challenges of ERT inversion, such as its under-determined nature and potential data errors, are addressed. Inversion algorithms and techniques are discussed, highlighting the iterative nature of the process and the importance of minimizing the misfit between observed and predicted data.

Furthermore, The model resolution analysis conducted for a range of synthetic scenarios offers valuable insights into the resolution quality achieved by the inversion technique. By systematically evaluating resolution matrices across different model configurations, considering the variable background resistivity, we gain a comprehensive understanding of the technique's effectiveness in imaging subsurface anomalies. These findings contribute to the ongoing refinement of inversion methodologies and enhance the reliability of subsurface imaging for various applications, including environmental monitoring, resource exploration, and geological characterization.

The study presents several synthetic models and corresponding inversion results, demonstrating the application of ERT inversion in different subsurface scenarios. These models showcase the ability of ERT inversion to provide insights into the spatial distribution and dynamic behavior of injected substances, such as CO_2, within subsurface environments. Overall, the comprehensive analysis presented in this study underscores the importance of ERT inversion in geophysical exploration and its potential for enhancing our understanding of subsurface geological structures and processes.

Chapter 6

Implementation and Analysis

This chapter will focus on the practical implementation of forward and inverse modeling techniques using MATLAB code. It will delve into the details of how the algorithms are applied and analyze the results obtained from the simulations. Additionally, it will discuss any challenges faced during the implementation and provide insights into the interpretation of the results.

- **Data Loading and Initialization:**

  1. Load necessary data files.
  2. Initialize parameters required for the inversion process.

  ```
  addpath('extra');
  addpath('GFCM');
  cen=[];
  models=[];
  inv_model=[];
  zone_model=[];
  models=[];
  mtype=0;
  itmax=5;
  ```

- **Reading and Preprocessing Data:**

  1. Read synthetic model data and apparent resistivity data.
  2. Set parameters for normalization, smoothing, and maximum depth.

  ```
  file='synthetic_model';
  data=read_data_grad([file,'.dat']);
  roa = xlsread('ro_data.csv');
  data.roa = roa;
  norm_p=2;
  epsilon=0.00001;
  alxx=0.02;
  data.zmax=140;
  alfax=1;
  alfaz=1;
  yky=1/data.zmax;
  ```

lambda=std(log(data.roa));

- **Setting Topography and Model Parameters:**
  1. Define topography coordinates.
  2. Set parameters for the inversion process like block sizes, noise, etc.

topx=-(data.xelek(end)-data.xelek(1))/2+2*data.ela:data.ela/2:(data.xelek(end)-data.xelek(1))/2-2*data.ela;

topy=zeros(size(topx));

grat0=1;

if min(topy)<0

   topy=topy-min(topy);

end

airz=100;

ntr=10;

nf=1;

per=1/19800;

freq=1./per;

rhoh=100;

hlfx=50;

hlfz=140;

xblock=200;

zblock=200;

noise=0.10;

- **Discretization and Initialization**:
  1. Generate a triangular mesh for the subsurface region.
  2. Perform initialization steps for the inversion process.

[gdd1,x1,z1,p,e,t]=discrunstrtri_inv(hlfx,hlfz,0.01,rhoh,airz,topx,topy,grat0,data);

ds=length(p);

es=length(t);

I=2*pi;

- **Triangular Mesh Generation:**
  1. Generate a triangular mesh for the subsurface region.

[delta,b1,c1,b2,c2,b3,c3]=pdetrgm(p,t);

- **Forward Modeling:**
  1. Perform forward modeling based on given parameters and data.
  2. Calculate forward-modeled data and Jacobian matrix.

% Perform forward modeling based on given parameters and data
% Calculate forward-modeled data and Jacobian matrix

% Initialize variables for forward modeling
[J,ro]=forward_anand(yky,t,es,real(sig),so,nel,akel,1,k1,x,V1,data,real(prho),npar,
p);
dd=log(data.roa(:))-log(ro(:));
misfit=sqrt((Rd*dd)'*(Rd*dd)/data.nd)*100;

- **Parameter Update:**
  1. Update model parameters iteratively using an inversion algorithm.
  2. Solve the linear system for parameter updates.

     % Update model parameters iteratively using an inversion algorithm
     % Solve the linear system for parameter updates
     % Damping factor
     while lambda<0.01
        lambda=0.01;
     end
     % Smoothness constrained least squares
     b=(J'*Rd'*Rd*dd-lambda*C*((1./prho(:))));
     A=(J'*Rd'*Rd*J+lambda*C);
     % Solve linear system for parameter updates
     setup = struct('type','ilutp','droptol',1e-6);
     [L,U] = ilu(sparse(A),setup);
     [dp,fl1,rr1,it1,rv1] = bicgstab(A,b,1e-6,20,L,U);
     fl1
     % Update model parameters
     parg=1./((1./prho(:)).*exp(dp));
     prho=parg';
     sig=1./prho;

- **Model Evaluation:**
  1. Evaluate the model and its resolution.

     % Evaluate the model and its resolution
     % Calculate model resolution
     RR=(inv(J'*Rd'*Rd*J+lambda*C))*(J'*Rd'*Rd*J);
     Model_resolution=abs(diag(RR));

```matlab
% Plot model resolution
figure
pdeplot(p,e,t,'xydata',log10(Model_resolution),'xystyle','flat','mesh','off');
xlabel('Distance (m)','fontweight','normal','fontsize',12);
ylabel('Depth (m)','fontweight','normal','fontsize',12);
set(gcf,'Position',[100 100 200 420])
```

References

Adeeko, T.O. and Samson, D.O., 2018. Application of electrical resistivity in mapping subsurface characteristics. *Asian Journal of Environment & Ecology, 6(2)*, pp.1-12.

Adhikari, P.K., Yadav, P.K., Srivastava, S., Maurya, V.P., Singh, S., Tripathi, A., Singh, R.K. and Bage, A.K., 2016. Near-surface high resolution imaging of a metallogenic zone in the northern fringe of Dalma volcanics in eastern India using electrical resistivity tomography. *Exploration Geophysics,* pp. 394-400.

Alumbaugh, D.L. and Newman, G.A., 2000. Image appraisal for 2-D and 3-D electromagnetic inversion. *Geophysics,* pp. 1455-1467.

Bing, Z. and Greenhalgh, S.A., 2000. Cross-hole resistivity tomography using different electrode configurations. *Geophysical prospecting,* pp. 887-912.

Bing, Z. and Greenhalgh, S.A., 2001. Finite element three dimensional direct current resistivity modelling: accuracy and efficiency considerations. *Geophysical Journal International,* pp. 679-688.

Binley, A. and Kemna, A., 2005. DC resistivity and induced polarization methods. *Hydrogeophysics,* pp. 129-156.

Candansayar, M.E., 2008. Two-dimensional individual and joint inversion of three-and four-electrode array dc resistivity data. *Journal of Geophysics and Engineering,* pp. 290-300.

Carrigan, M., Moraes, C. and McEachern, M., 2013. From conspicuous to considered fashion: A harm-chain approach to the responsibilities of luxury-fashion businesses. *Journal of Marketing Management,* pp. 1277-1307.

Chen, H., 2022. Exploring subsurface hydrology with electrical resistivity tomography. *Nature Reviews Earth & Environment,* pp. 813-813.

Daily, W. and Owen, E., 1991. Cross-borehole resistivity tomography. *Geophysics,* pp. 1228-1235.

Ekblom, H., 1987. The L1-estimate as limiting case of an Lp-or Huber-estimate. *Statistical data analysis based on the L1-norm and related methods,* pp. 109-116.

Falcon-Suarez, I., Marín-Moreno, H., Browning, F., Lichtschlag, A., Robert, K., North, L.J. and Best, A.I., 2017. Experimental assessment of pore fluid distribution and geomechanical changes in saline sandstone reservoirs during and after CO2 injection. *International Journal of Greenhouse Gas Control,* pp. 356-369.

Hayley, K., Bentley, L.R., Gharibi, M. and Nightingale, M., 2007. Low temperature dependence of electrical resistivity: Implications for near surface geophysical monitoring. *Geophysical research letters,* 18(34).

Ishizu, K., Goto, T., Ohta, Y., Kasaya, T., Iwamoto, H., Vachiratienchai, C., Siripunvaraporn, W., Tsuji, T., Kumagai, H. and Koike, K., 2019. Internal structure of a seafloor massive sulfide deposit by electrical resistivity tomography, Okinawa Trough. *Geophysical Research Letters, 46(20),* pp. 11025-11034.

Krishan, G., Rao, M.S., Kumar, C.P., Kumar, S. and Rao, M.R.A., 2015. A study on identification of submarine groundwater discharge in Northern East Coast of India. *Aquatic Procedia,* pp. 3-10.

La Brecque, D., Daily, W. and Adkins, P., 2007 Systematic errors in resistivity measurement systems. *Symposium on the Application of Geophysics,* pp. 1153-1160.

Li, T., Gu, Y.J., Lawton, D.C., Gilbert, H., Macquet, M., Savard, G., Wang, J., Innanen, K.A. and Yu, N., 2022. Monitoring CO2 injection at the CaMI Field Research Station using microseismic noise sources. *Journal of Geophysical Research: Solid Earth.*

Masood, A., Tariq, M.A.U.R., Hashmi, M.Z.U.R., Waseem, M., Sarwar, M.K., Ali, W., Farooq, R., Almazroui, M. and Ng, A.W., 2022. An overview of groundwater monitoring through point-to satellite-based techniques. *Water,* p. 565.

Menke, W., 1989. *Geophysical data analysis: Discrete inverse theory (revised).* San Diego: Academic Press.

Wiwattanachang, N. and Giao, P.H., 2011. Monitoring crack development in fiber concrete beam by using electrical. *Journal of Applied Geophysics,* p. 294–304.

Nassir, S.A., Loke, M.H., Lee, C.Y. and Nawawi, M.N.M., 2000. Salt-water intrusion mapping by geoelectrical imaging surveys. *Geophysical Prospecting,* pp. 647-661.

Newmark, R.L., Ramirez, A.L. and Daily, W.D., 2003. Monitoring carbon dioxide sequestration using electrical resistance tomography (ERT): A minimally invasive method. *Greenhouse Gas Control Technologies-6th International Conference,* pp. 353-358.

Okiongbo, K.S. and Ogobiri, G., 2013. Predicting soil corrosivity along a pipeline route in the Niger Delta Basin using geoelectrical method: Implications for corrosion control. *Engineering,* pp. 5-237.

Oldenburg, D.W., Li, Y., Farquharson, C.G., Kowalczyk, P., Aravanis, T., King, A., Zhang, P. and Watts, A., 1998. Applications of geophysical inversions in mineral exploration. *The Leading Edge,* pp. 461-465.

Prakash, A. and Bharati, A.K., 2022. Implication of electrical resistivity tomography for precise demarcation of pothole subsidence potential zone over shallow depth coal mine workings. *Journal of the Geological Society of India,* pp. 600-606.

Raab, T., Weinzierl, W., Wiese, B., Rippe, D. and Schmidt-Hattenberger, C., 2020. Development of an Electrical Resistivity Tomography Monitoring Concept for the Svelvik CO 2 Field Lab, Norway. *Advances in Geosciences,* pp. 41-53.

Schmidt-Hattenberger, C., Bergmann, P., Bösing, D., Labitzke, T., Möller, M., Schröder, S., Wagner, F. and Schütt, H., 2013. Electrical resistivity tomography (ERT) for monitoring of CO_2 migration-from tool development to reservoir surveillance at the Ketzin pilot site. *Energy Procedia,* pp. 4268-4275.

Sikandar, P., Bakhsh, A., Ali, T. and Arshad, M., 2010. Vertical electrical sounding (VES) resistivity survey technique to explore low salinity groundwater for tubewell installation in Chaj Doab. *Journal of Agricultural Research,* pp. 1-48.

Tsai, W.N., Chen, C.C., Chiang, C.W., Chen, P.Y., Kuo, C.Y., Wang, K.L., Lin, M.L. and Chen, R.F., 2021. Electrical resistivity tomography (ERT) monitoring for landslides: Case study in the lantai area, yilan taiping mountain, northeast taiwan. *Frontiers in Earth Science,* p. 737271.

Wagner, F.M. and Wiese, B.U., 2018. Fully coupled inversion on a multi-physical reservoir model–Part II: The Ketzin CO_2 storage reservoir. *International Journal of Greenhouse Gas Control,* pp. 273-281.

Wilson, B., Singh, A. and Sethi, A., 2022. Appraisal of Resistivity Inversion Models With Convolutional Variational Encoder–Decoder Network. *IEEE Transactions on Geoscience and Remote Sensing, 60,,* pp. 1-10.